



TRABAJO FINAL DE MASTER
Development of Dy-free, high coercivity
Nd-Fe-B magnets

Presentado por:
Andrés Martín Cid

Realizado en:
Dpto. Electricidad y Electrónica (UPV/EHU)
BCMaterials



Bajo la dirección de:
José Manuel Barandiarán García (UPV/EHU)
Daniel Salazar Jaramillo (BCMaterials)

Leioa, Julio 2015

Acknowledgements

This work was done at the Basque Center for Materials, Applications & Nanostructures under the direction of José Manuel Barandiarán García who I want to thank for the invested time and support given. I would like to thank Daniel Salazar Jaramillo for his patience and hard work helping to make this work. Special thanks to Professor George C. Hadjipanayis from the department of Physics and Astronomy at the University of Delaware for his fruitful help and for sharing his knowledge.

At last, thanks to people from the department of Electricity and Electronics and department of Inorganic Chemistry of the University of Basque Country (UPV/EHU) and the General Services of the UPV/EHU (SGIKER) for the measurements of X-ray diffraction and VSM, especially to Dr. Aitor Larrañaga Varga and Dr. Iñaki Orue Goikuria.

Abstract

This project is focused on the development of high coercivity rare earth-lean/ Dy-free Nd-Fe-B permanent magnets using grain boundary engineering and the analysis of their microstructure and magnetic properties. The experiments were performed on the understoichiometric Nd-lean ($\text{Nd}_{10}\text{Fe}_{84}\text{B}_6$) and the stoichiometric ($\text{Nd}_{12}\text{Fe}_{81}\text{B}_6\text{Nb}_1$) composition and using the low melting point $\text{Pr}_3\text{Co}_{0.75}\text{Cu}_{0.25}$ eutectic alloy as infiltration material.

Different heat treatments were carried out on initial amorphous ribbons to find out an optimal grain size with highest coercivity. The best sample obtained (650 °C – 1h) was used to diffuse PrCoCu alloy at 600 °C for several times. After 4 hours of infiltration time the coercivity of modified magnet was increased from 5 kOe up to 24.4 kOe. Microstructure were analysed by X-ray diffraction (XRD). Modified grain boundary of magnet with highest coercivity was observed by scanning transmission electron microscopy (STEM) and the magnetic properties were analysed by high field - vibrating sample magnetometer (HF-VSM 12T).

Resumen

Este Proyecto está enfocado al desarrollo de imanes permanentes con alto campo coercitivo de Nd-Fe-B con escasez de tierras raras y libres de Dy usando ingeniería de frontera de grano y el análisis de su microestructura y propiedades magnéticas. Los experimentos han sido realizados en la composición no estequiométrica con escasez de Nd ($\text{Nd}_{10}\text{Fe}_{84}\text{B}_6$) y en la estequiométrica ($\text{Nd}_{12}\text{Fe}_{81}\text{B}_6\text{Nb}_1$) y usando como material para infiltra la aleación eutéctica de bajo punto de fusión $\text{Pr}_3\text{Co}_{0.75}\text{Cu}_{0.25}$.

Se han realizado diferentes tratamientos térmicos en las cintas amorfas iniciales para buscar el tamaño de grano óptimo con la mayor coercitividad. La mejor muestra obtenida (650 °C – 1h) se utilizó para difundir la aleación de PrCoCu a 600 °C durante diversos tiempos. Tras 4 horas de infiltración la coercitividad de los imanes modificados se incrementó de 5 kOe hasta 24.4 kOe. La microestructura ha sido analizada por difracción de rayos X (XRD). La frontera de grano modificada del imán con mayor coercitividad fue observad por microscopia electrónica de barrido-transmisión (STEM) y las propiedades magnéticas se analizaron por un magnetómetro de muestra vibrante de alto campo (HF-VSM 12T).

Table of contents

ACKNOWLEDGEMENTS	I
ABSTRACT.....	II
LIST OF FIGURES.....	IV
LIST OF TABLES	V
1. INTRODUCTION.....	1
1.1. MOTIVATION.....	1
1.2. CONCEPTS ON MAGNETISM.	4
1.2.1. <i>Magnetic anisotropy</i>	4
1.2.2. <i>Permanent magnets properties</i>	6
1.2.3. <i>Nanocomposite exchange-coupled magnets</i>	10
1.2.4. <i>Commercial magnets available</i>	12
1.3. OBJECTIVES.	13
2. EXPERIMENTAL METHODOLOGY.....	14
2.1. FABRICATION TECHNIQUES.	14
2.1.1. <i>Arc-Melting & Melt-spinning</i>	14
2.1.2. <i>Thermal treatments</i>	14
2.2. CHARACTERIZATION TECHNIQUES.....	14
2.2.1. <i>Differential thermal analysis (DTA)</i>	14
2.2.2. <i>X-ray diffraction (XRD)</i>	15
2.2.3. <i>Vibrating sample magnetometer (VSM)</i>	16
2.2.4. <i>Scanning transmission electron microscopy (STEM)</i>	17
3. RESULTS & DISCUSSION	18
3.1. NANOCRYSTALLINE HARD MAGNETS.	18
3.2. COERCIVITY ENHANCEMENT BY GRAIN BOUNDARY ENGINEERING.	22
3.2.1. <i>Magnetic properties</i>	22
3.2.2. <i>Microstructure</i>	26
4. CONCLUSIONS.....	30
5. BIBLIOGRAPHY	31

List of figures

FIGURE 1.1.- WORLD DISTRIBUTION OF RARE EARTH PRODUCTION AND ESTIMATED RESERVES.	2
FIGURE 1.2.- EVOLUTION OF RE OXIDE PRICES BETWEEN 2008 AND 2013 (US \$/KG) [8].....	2
FIGURE 1.3.- U.S. MEDIUM-TERM (2015-2025) CRITICALITY MATRIX [6].....	3
FIGURE 1.4.- INTERACTION BETWEEN SPIN AND ORBIT DEGREES OF FREEDOM [12].	4
FIGURE 1.5.- H FIELD AROUND A PROLATE SPHEROID [12].	5
FIGURE 1.6.- HYSTERESIS LOOP [12].....	6
FIGURE 1.7.- DISTRIBUTION OF DOMAIN ORIENTATIONS AT VARIOUS POINTS ALONG A HYSTERESIS LOOP [12].....	7
FIGURE 1.8.- OPEN MAGNETIC CIRCUIT [10].	8
FIGURE 1.9.- LEFT: DEMAGNETIZATION CURVE; RIGHT: CORRESPONDING VALUES OF ENERGY PRODUCT (BH) PLOTTED ON THE SAME B SCALE. MAXIMUM VALUE OF (BH) IS SHOWN ON BOTH PLOTS [12].	9
FIGURE 1.10.- EVOLUTION OF MAXIMUM ENERGY PRODUCT OVER THE LAST CENTURY.	10
FIGURE 1.11.- SCHEMATIC ONE-DIMENSIONAL MODEL OF THE MICROSTRUCTURE AND THE MICROMAGNETIC STRUCTURE OF THE EXCHANGE-COUPLED COMPOSITE MAGNET DEMAGNETIZATION. THE BLUE ARROWS REPRESENTS THE HARD PHASE WHILE THE BROWN REPRESENTS THE SOFT PHASE.	10
FIGURE 1.12.- SCHEMATIC HYSTERESIS LOOPS OF THE MIXTURE OF THE HARD PHASE AND THE SOFT PHASE.	11
FIGURE 1.13.- (A) SCHEMATIC DEMAGNETIZATION CURVES FOR AN EXCHANGE SPRING MAGNET AND A CONVENTIONAL MAGNET AND (B) SCHEMATIC REPRESENTATION OF THE REVERSIBILITY OF THE MAGNETIC MOMENTS.	11
FIGURE 1.14.- COERCIVITY (H_{cJ}) AND RESIDUAL INDUCTION (B_R) AS A FUNCTION OF DYSPROSIUM CONTENT. ON TOP, APPLICATIONS FOR EACH GRADE [23].	12
FIGURE 2.1.- SCHEMATIC BASIC OPERATION OF A VSM.	17
FIGURE 3.1.- DTA CURVE FOR THE COMPOSITIONS $ND_{10}FE_{84}B_6$ (RED LINE) AND $ND_{12}FE_{81}B_6ND_1$ (BLUE LINE).....	18
FIGURE 3.2.- HYSTERESIS LOOPS OF THE AMORPHOUS AND NANOCRYSTALLINE RIBBONS. LEFT: $ND_{10}FE_{84}B_6$ COMPOSITION, RIGHT: $ND_{12}FE_{81}B_6NB_1$ COMPOSITION.....	19
FIGURE 3.3.- SIZE DEPENDENCE OF COERCIVITY [13].....	19

FIGURE 3.4.- COERCIVE FIELD OF THE DIFFERENT HEAT TREATED SAMPLES. LEFT: $\text{Nd}_{10}\text{Fe}_{84}\text{B}_6$ COMPOSITION, RIGHT: $\text{Nd}_{12}\text{Fe}_{81}\text{B}_6\text{Nb}_1$ COMPOSITION..... 20

FIGURE 3.5.- DIFFRACTOGRAMS OF THE SAMPLES HEAT TREATED AT 650 °C OF $\text{Nd}_{10}\text{Fe}_{84}\text{B}_6$ (UP) AND AT 700 °C OF $\text{Nd}_{12}\text{Fe}_{81}\text{B}_6\text{Nb}_1$ (DOWN). THE PEAK CORRESPONDING WITH THE A-FE PHASE IS INDICATED. 21

FIGURE 3.6.- (A) HYSTERESIS LOOPS OF THE INFILTRATED SAMPLES AFTER DIFFERENT DIFFUSION TREATMENT TIMES AT 600 °C AND (B) DETAILED DEMAGNETIZATION CURVES..... 22

FIGURE 3.7.- EVOLUTION OF THE REMANENCE SATURATION RATIO WITH THE DIFFUSION PROCESS TIME. 23

FIGURE 3.8.- ΔM CURVES FOR THE NANOCRYSTALLINE (RED) AND THE 4 HOURS DIFFUSED (BLACK) SAMPLES..... 24

FIGURE 3.9.- EVOLUTION OF THE COERCIVITY WITH THE DIFFUSION PROCESS TIME. 25

FIGURE 3.10.- XRD DIFFRACTOGRAMS REFINED WITH FULLPROF OF THE NANOCRYSTALLINE SAMPLE (TOP), THE 2 HOUR DIFFUSED SAMPLE (MIDDLE) AND THE 4 HOURS DIFFUSED SAMPLE (DOWN). ANALYSED PHASES: $\text{Nd}_2\text{Fe}_{14}\text{B}$ (BLUE), A-FE (RED) AND PR₂CU (GREEN). 27

FIGURE 3.11.- HIGH ANGULAR ANNULAR DARK-FIELD IMAGE (STEM-HAADF) OF THE 4 HOURS DIFFUSED SAMPLE. 28

FIGURE 3.12.- TEM IMAGES OF THE SAMPLED DIFFUSED FOR 4 HOURS. 28

FIGURE 3.13.- STEM-EDS ELEMENTAL MAPPING IMAGES OF THE 4 HOURS DIFFUSED SAMPLE..... 29

List of tables

TABLE 3.1.- COMPARISON OF COERCIVITY FROM DIFFERENT PERMANENT MAGNETS, COMMERCIALY AVAILABLE (C) AND FROM LABORATORY (L)..... 25

TABLE 3.2.- AMOUNT OF A-FE PHASE IN THE DIFFERENT DIFFUSED SAMPLES. 26

1. Introduction.

1.1. Motivation.

Nowadays permanent magnets are indispensable for many commercial and military applications. Major commercial applications include the electric, electronic and automobile industries, communications, information technologies and automatic control engineering. These applications can be divided in four categories [1] according to the kind of use of the magnetic field of the magnet, which are the tractive and/or repelling force of the magnet used to do mechanical work (category 1), to convert mechanical energy to electrical energy (category 2), to convert electrical energy to mechanical energy (category 3) and to control the shape and direction of electron/ion beams (category 4).

Category 1 include applications such as magnetic separators, magnetic holding devices, magnetic torque drives and magnetic bearing devices. Category 2 comprise magnetos, generators and alternators and Eddy current brakes. Category 3 applications are motors, meters, loudspeakers, relays and actuators. Finally, category 4 includes magnetic focused cathode-ray tubes, traveling wave tubes, magnetrons, backward wave oscillator, klystrons, ion pumps and cyclotrons.

This extensive list of permanent magnets applications is due to their several advantages over conventional (current-driven) electromagnets. The most important advantage is that they can provide a relatively strong magnetic field over an extended spatial region for an indeterminate period of time with no use of energy. Another advantage is that they can be fabricated with a wide range of structural properties, geometrical shapes, and magnetization patterns.

The global market for permanent magnets (PM) is projected to reach US\$18,800 billion by the year 2018. The number one risk to the permanent magnet industry is their dependency in rare earth elements (RE), and hence should be avoided or minimised in the search for new materials. Virtually in every application, an increase in the magnetic energy density of the magnet, usually presented via the maximum energy product $(BH)_{max}$ [2], immediately increases the efficiency of the whole device (a typical example is the volume-to-power ratio of an electric motor). Moreover, for many applications (such as MRI), it is the high $(BH)_{max}$ which enables the use of permanent magnets instead of less efficient alternatives (like energy consuming electromagnets). Energy-saving hybrid cars, emerging electric cars and wind power are expected to be among the major consumers of high-energy permanent magnets.

These magnets are also expected to play essential role in a number of proposed energy-saving technologies, such as the MagLev trains, the magnetic refrigeration and the flywheel energy storage [3].

All commercially available high energy permanent magnets contain rare earth elements. The RE market has become increasingly tight and is now dominated by China, which possesses and uses most of the world's RE resources (see Figure 1.1). Restrictions on the export of RE placed by China in 2010 led to a temporary rare earth crisis that resulted in drastic increase in RE costs for a couple of years.

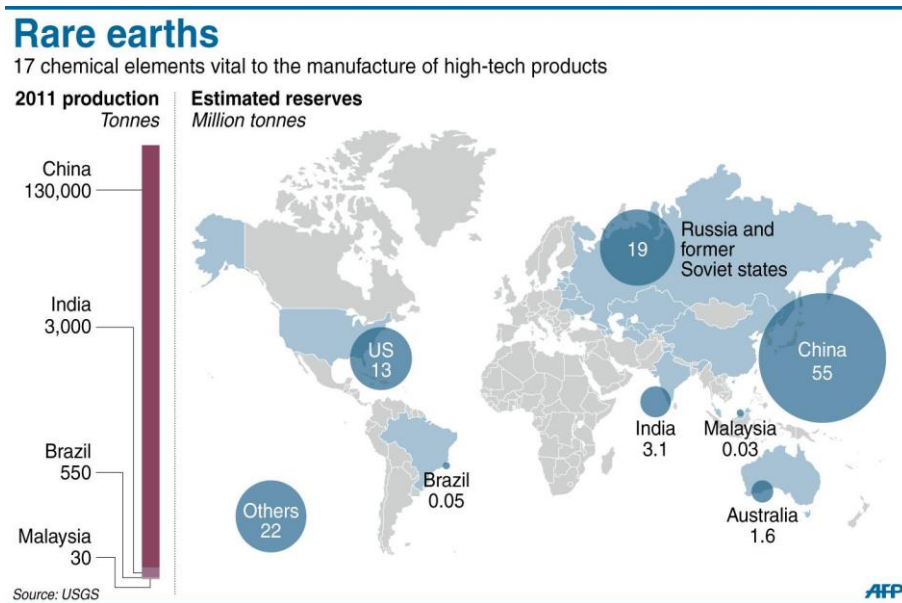


Figure 1.1.- World distribution of rare earth production and estimated reserves.

Figure 3. Selected Rare Earth Oxide Prices, 2008-2013

(US \$/kg)

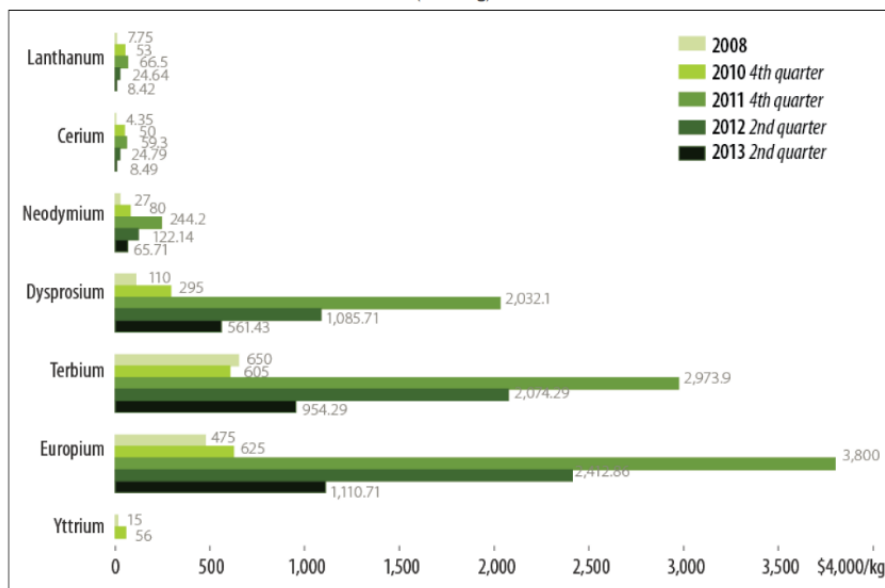


Figure 1.2.- Evolution of RE oxide prices between 2008 and 2013 (US \$/kg) [8].

Among all available permanent magnets, Nd-Fe-B magnets with some added dysprosium (Dy) are the most powerful magnets in the temperature range up to 200 °C with a high remanence and a high coercivity ($\mu_0 H_c > 2T$) [4]. The Dy-containing Nd-Fe-B magnets are far more expensive than other lower-grade rare-earth-less types of magnets, but still affordable enough to be widely used in industry: an electrical car contains about 2 kg of $Nd_2Fe_{14}B$ (of which 8 to 12 % is Dy), while a single wind turbine devours up to 1 ton (of which 4% is Dy) of these high-quality magnets. These demands are rapidly depleting the already compromised existing rare earth resources to the limit of jeopardising the supply of existing needs, particularly dysprosium and terbium, internationally identifying them as critical raw materials (CRM) [5] [6].

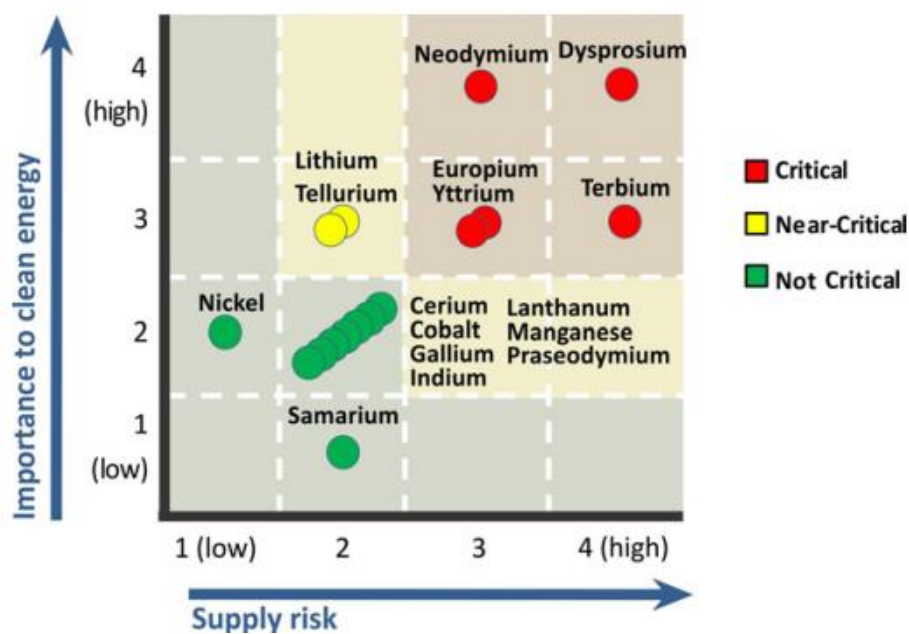


Figure 1.3.- U.S. medium-term (2015-2025) criticality matrix [6].

This uncertainty in RE market resulted in worldwide efforts to develop RE-lean/free magnets. In RE-lean magnets large efforts have been focused nanocomposite spring magnets consisting of a fine mixture of magnetically hard (Sm-Co, Nd-Fe-B) and soft or semi hard phases (Fe, Co, Fe_3B) [7] exchange coupled to the hard phases. So far, the only success has been reported in epitaxial multilayers but not in particles/powders that can be used to make bulk magnets.

1.2. Concepts on magnetism.

1.2.1. Magnetic anisotropy.

When the magnetic properties of a material depends on the direction in which they are measured it can be said that magnetic anisotropy exists. This property can be intrinsic to the material (*magnetocrystalline anisotropy*) or induced; like the shape anisotropy.

Magnetocrystalline anisotropy is the tendency of the magnetization to align itself along a preferred crystallographic direction, called the “easy” axes, since it is easiest to magnetize a demagnetized sample to saturation if the external field is applied along a preferred direction. The crystal is higher in energy when the magnetization points along the hard direction than along the easy direction, and the energy difference per unit volume between samples magnetized along easy and hard directions is called the magnetocrystalline anisotropy energy.

The energy required to rotate the spin system of a domain away from the easy direction is actually the energy required to overcome the spin-orbit coupling. When an applied field tries to reorient the direction of the electron spin, the orbital also needs to be reoriented, because of the coupling between the spin and orbital components. However, the orbital is in general also strongly coupled to the lattice, and so the attempt to rotate the spin axis is resisted. This is illustrated schematically in Figure 1.4. Part (a)

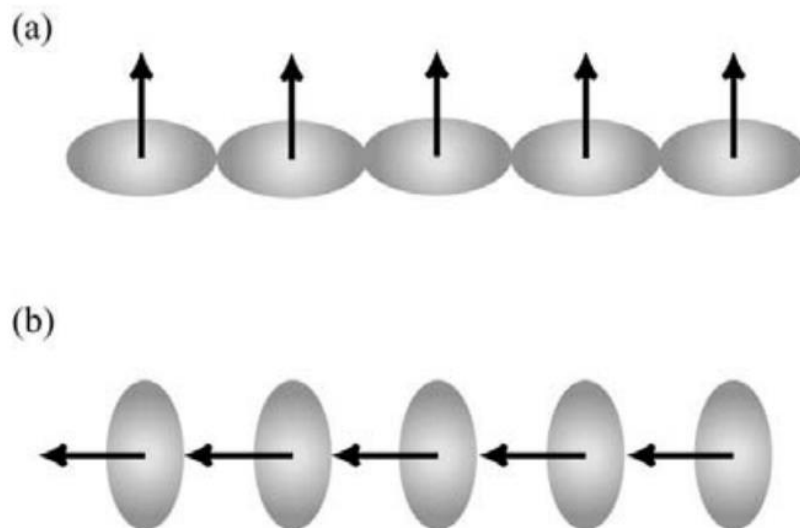


Figure 1.4.- Interaction between spin and orbit degrees of freedom [12].

shows the magnetic moments aligned along the easy (vertical) axis, with the orbital components, which are not spherical because of the spin–orbit coupling, aligned with their long axes along the horizontal axis. For this particular crystal this orbital arrangement is energetically favourable. Part (b) shows the result of forcing the

magnetic spins to align along the horizontal axis by applying an external magnetic field. The orbital components no longer have favourable overlap with each other or with the lattice.

In most materials this anisotropy is very weak, but it is really strong in rare earths due to the strong spin-orbit coupling. This translates in the necessity to apply a large magnetic field in the opposite direction of a magnetized sample in order to overcome the anisotropy and reverse the magnetization.

Although most materials show some magnetocrystalline anisotropy, a polycrystalline sample with no preferred orientation of its grains will have no overall crystalline anisotropy. However, only if the sample is exactly spherical will the same field magnetize it to the same extent in every direction. If the sample is not spherical, then it will be easier to magnetize it along a long axis. This phenomena is known as shape anisotropy.

It is necessary to introduce the concept of demagnetizing field in order to understand the origin of shape anisotropy. Let's suppose that a prolate spheroid has been

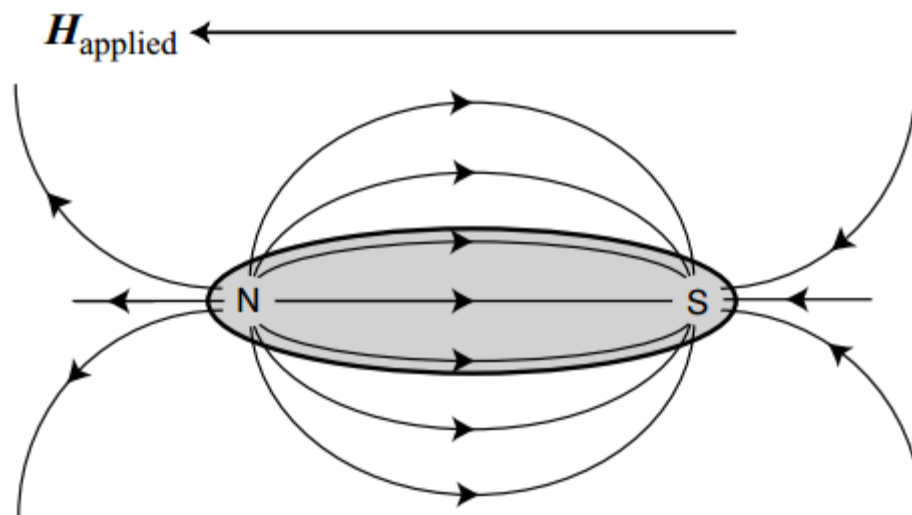


Figure 1.5.- H field around a prolate spheroid [12].

magnetized by a magnetic field applied from right to left. This results in a north pole at the left end of the prolate spheroid and a south pole at the right end. By definition, the lines of H radiates from the north pole and ends at the south pole, resulting in the pattern of field lines shown in Figure 1.5. We see from the figure that the field inside the sample points from left to right, that is, in the opposite direction to the applied external field. This internal field tends to demagnetize the magnet, and so we call it the demagnetizing field, H_d . The demagnetizing field is created by the magnetization of the sample, and in fact the size of the demagnetizing field is directly proportional to the size of the magnetization. We write:

$$H_d = N_d M \quad (1.1)$$

where N_d is called the demagnetizing factor, and is determined by the shape of the sample. For elongated samples, N_d is smallest along the long axis and largest along the short axis. The anisotropy becomes stronger as the aspect ratio increases.

Moreover, the effective field inside the material, H_{eff} is smaller than the applied field by an amount equal to the magnetizing field:

$$H_{eff} = H_{applied} - H_d \quad (1.2)$$

So along the long axis, where N_d is small, most of the applied field goes into magnetizing the sample. By contrast, along the short axis N_d is large, so most of the applied field goes into overcoming the demagnetizing field. As a consequence it is easier to magnetize the sample along the long axis.

1.2.2. Permanent magnets properties.

The macroscopic or bulk magnetic properties of a material are expressed in graphical form by plotting the magnetization \mathbf{M} or the magnetic induction \mathbf{B} as a function of the external field applied \mathbf{H} . It is possible to convert between either of these plots using the constitutive relation $\mathbf{B} = \mu_0(\mathbf{H} + \mathbf{M})$.

The B-H plot is called a hysteresis loop, and as can be seen in Figure 1.6 it is nonlinear and multivalued, reflecting the fact that the response of a material depends on its prior state of magnetization.

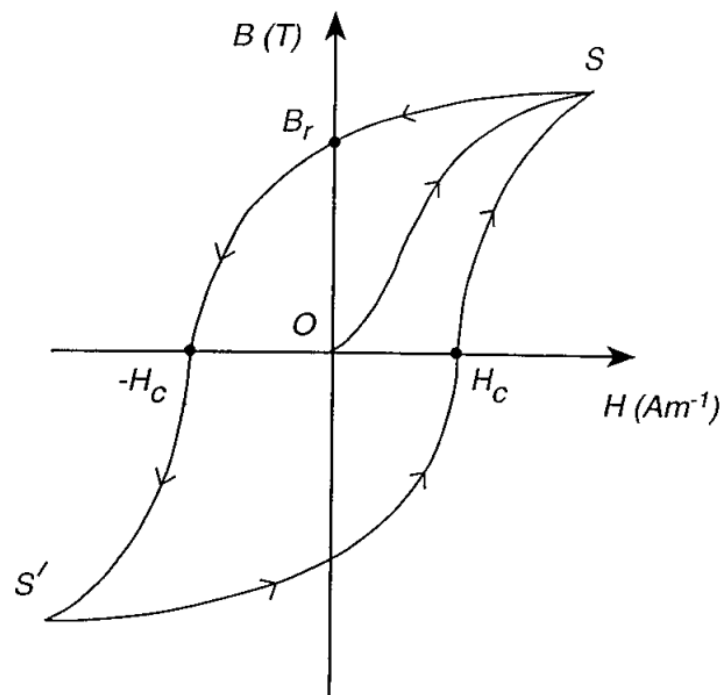


Figure 1.6.- Hysteresis loop [12].

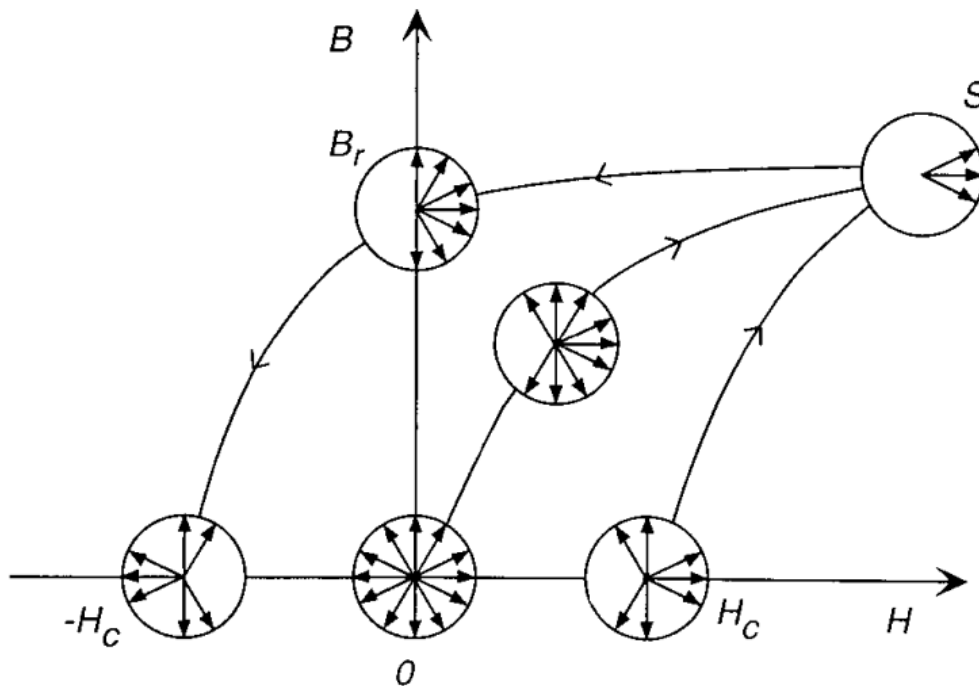


Figure 1.7.- Distribution of domain orientations at various points along a hysteresis loop [12].

Consider a sample with an isotropic distribution of preferred axes orientations. At first, it is demagnetized with its domains isotropically oriented as shown at point O in Figure 1.7. Applying an H-field, as H increases, the domains aligned with H grow, and the unaligned shrink due to the domain wall motion. As H increases further, the magnetic moments in the remaining unaligned domains rotate (or flip) into alignment along preferred axes that are in the general direction of H. When H reaches a certain value, all the magnetic moments rotate from their preferred axes that are not strictly aligned with H to align with the field (point S) (Figure 1.6 and Figure 1.7). At this point the material has reached its saturation induction B_s (or saturation magnetization M_s). The segment OS is called the initial magnetization curve.

As H is reduced from the saturation value, the moments along preferred axes aligned with H retain their orientation while the moments in domains with easy axis offset from H rotate back towards the nearest easy axis, away from H. This results in a distribution of domain alignments about the plus direction even when H is reduced to zero, exhibiting a remanent induction B_r (or magnetization M_r) (Figure 1.7).

If H is reversed, the moments in domains orientated along the plus direction rotate into alignment along the negative direction. There is a point where the reversed H rotates a sufficient number of domains to the negative orientation offsetting the magnetization of the remaining positively orientated domains so that the net induction in the sample is zero. This value of H is called the coercivity and is denoted H_c . As H increases in the negative direction, more domains reverse their orientation, reaching

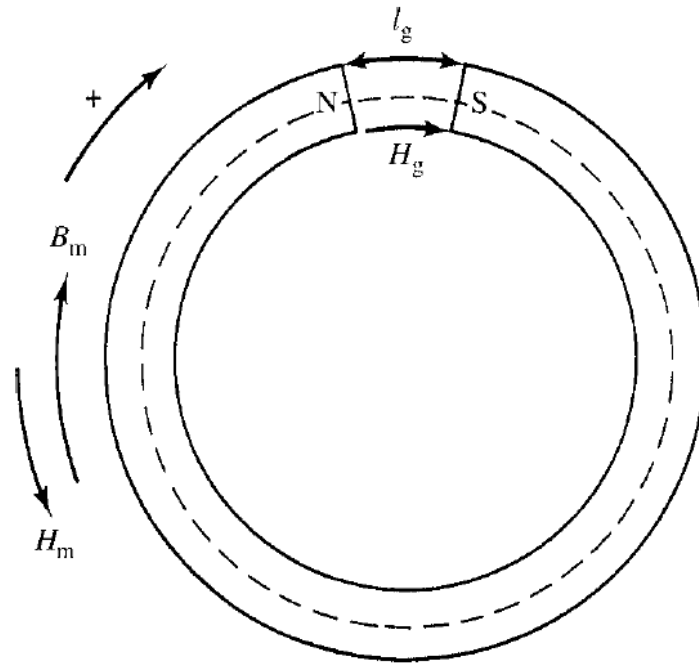


Figure 1.8.- Open magnetic circuit [10].

finally saturation. From this point, as H is decreased and then increases in the positive direction, the same phenomena occurs until reaching again the saturation state, closing the cycle.

The purpose of a permanent magnet is to provide a magnetic field in a particular volume of space, because of this, it must have free poles. One way of measuring the performance of a permanent magnet is the maximum energy product $(BH)_{max}$.

Consider the specific case of the gapped ring of Figure 1.8. The magnet must provide a field H_g of constant strength in the air gap. The induction in the magnet is B_m and the field is H_m . According to Ampere's law, the line integral of H around the ring must be zero, because there is no current flowing (Equation 1.1).

$$\oint H dl = 0, \quad (1.3)$$

$$H_g l_g - H_m l_m = 0, \quad (1.4)$$

where l_m is the length of the magnet and l_g is the length of the gap. The continuity of the lines of B give us a second equation:

$$\phi = B_g A_g = H_g A_g = B_m A_m \text{ (cgs)} \quad (1.5)$$

$$\phi = B_g A_g = \mu_0 H_g A_g = B_m A_m \text{ (SI)}$$

because $B = H$ (cgs) or $\mu_0 H$ (SI) in the air gap. Here A_g and A_m are the cross-sectional areas of the air gap and the magnet. In Figure 1.8 these are equal, because fringing of the flux in the gap is ignored.

If Equations 1.2 and 1.3 are each solved for H_g and multiplied together, we find

$$H_g^2 = \frac{B_m H_m l_m A_m}{l_g A_g}, \quad (1.6)$$

$$H_g^2 V_g = (B_m H_m) V_m,$$

where V stands for volume. This result shows that the volume $V_m = A_m l_m$ of a magnet is required to produce a given field in a given gap is a minimum when the product BH in the magnet is maximum. The energy stored in the field in the air gap is $H_g^2 V_g / 8\pi$ ergs (cgs) or $\mu_0 H_g^2 V / 2$ joule (SI). For a magnet of any volume, this energy is directly proportional to BH , which is called the energy product. Figure 1.7 shows how BH varies with B over the demagnetization curve, going through a maximum value $(BH)_{\max}$ for a particular value of B.

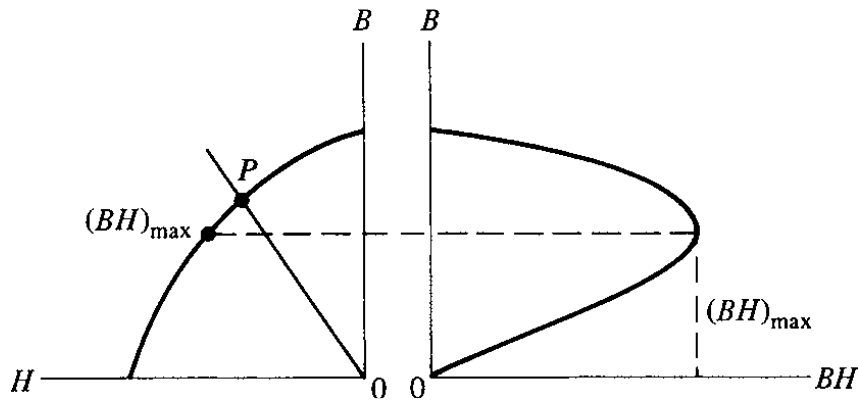


Figure 1.9. - Left: demagnetization curve; right: corresponding values of energy product (BH) plotted on the same B scale. Maximum value of (BH) is shown on both plots [12].

Over the last century the maximum energy product has increased by a factor of 100 as shown in Figure 1.10. There is two improvement steps that worth mention. The first step was at the 60s with the development of the first rare earth permanent magnet based on SmCo and later with the SmTM magnets, reaching maximum energy product up to 32 MGOe. The second big step happened in the 80s with the development of the NdFeB magnets, reaching maximum energy product close to 60 MGOe with the addition of some Dysprosium.

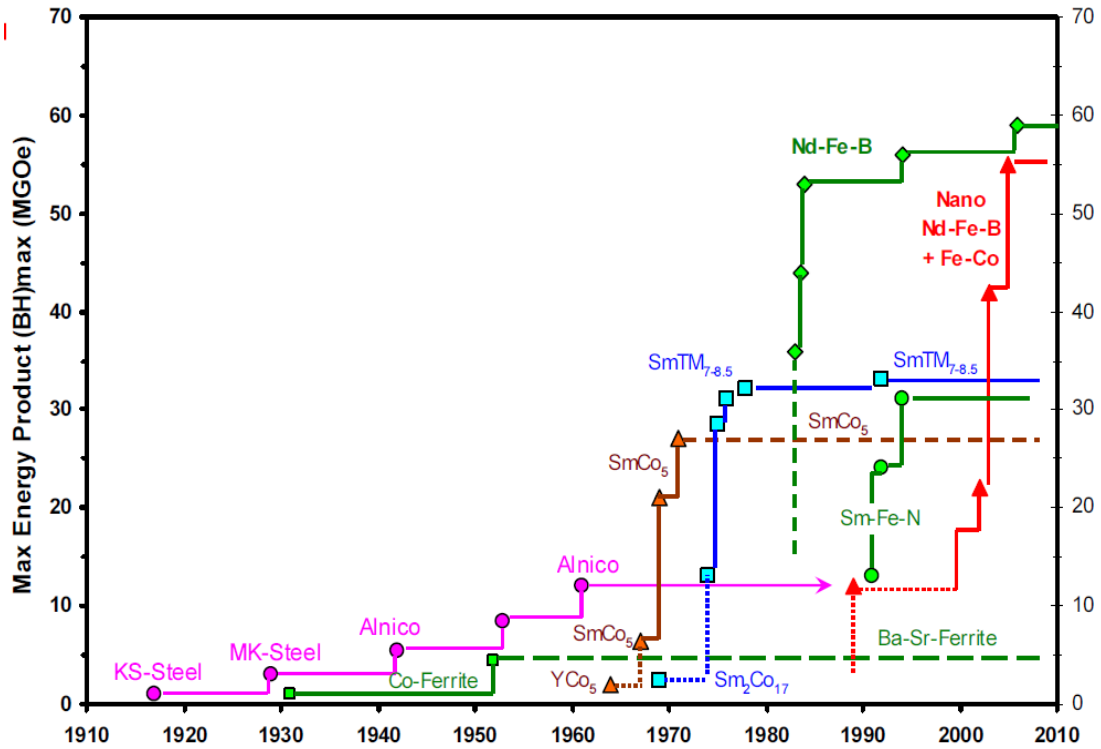


Figure 1.10.- Evolution of maximum energy product over the last century.

1.2.3. Nanocomposite exchange-coupled magnets.

Nanocomposite exchange-coupled magnets consists of a fine mixture of magnetically hard (to provide high coercivity) and soft (to provide high magnetization) phases. This kind of magnets was first experimentally observed by Coehoorn et al. [8] and later Kneller and Hawig [7] proposed a theoretical treatment for them. Their theoretical treatment was based on a one-dimensional model with alternating hard and soft regions. Figure 1.11 shows the schematic hard/soft/hard trilayer structure with inter-phase exchange-coupling. When the soft phase layer (middle layer) is thin enough, magnetic moments in both layers will be switched coherently.

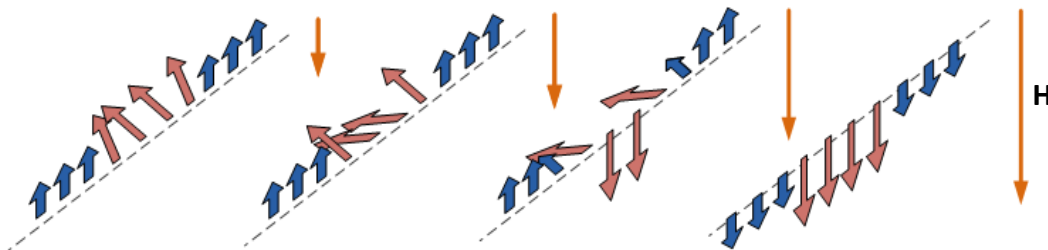


Figure 1.11.- Schematic one-dimensional model of the microstructure and the micromagnetic structure of the exchange-coupled composite magnet demagnetization. The blue arrows represents the hard phase while the brown represents the soft phase.

Kneller and Hawig also discussed that the general shape of the hysteresis loop for an exchange coupled magnet with optimum microstructure (fine mixture) should be similar to a conventional permanent magnet, while if there was no exchange coupling it would be a constricted loop (coarse mixture) (see Figure 1.12).

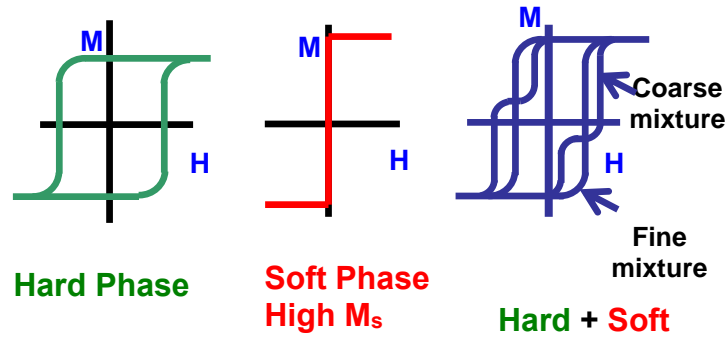


Figure 1.12.- Schematic hysteresis loops of the mixture of the hard phase and the soft phase.

Another feature of this kind of magnets is that the demagnetization curve after previous saturation will be reversible in reverse fields $H < H_{n0}$, i.e., before the magnetization of the hard phase begins to switch as illustrated schematically in Figure 1.13. Is because this typical magnetic behaviour, resembling a mechanical spring, that such magnets have been named exchange-spring magnets. Their unusual reversibility in

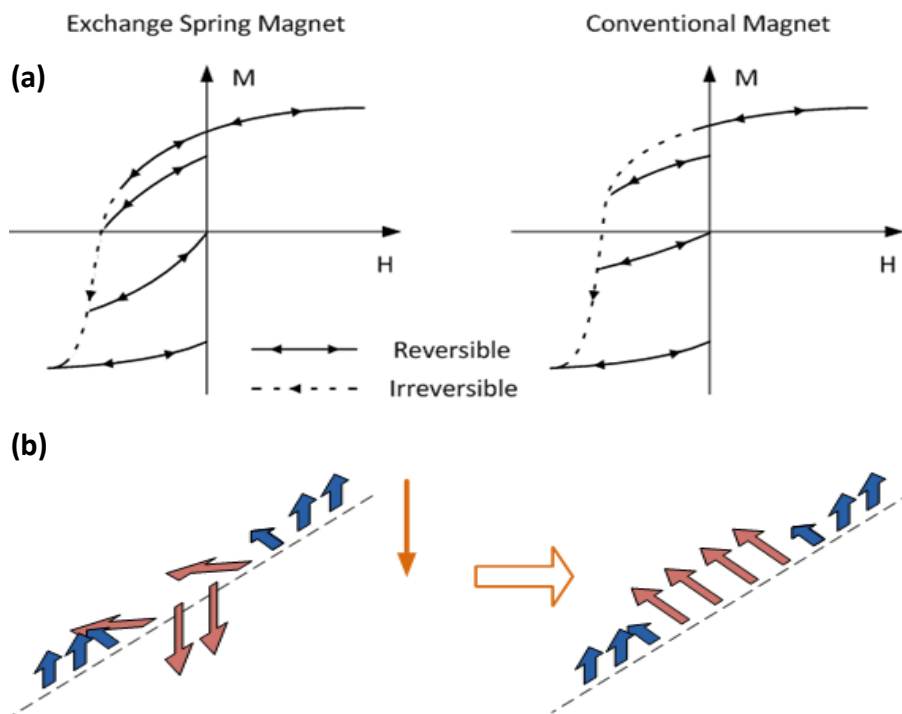


Figure 1.13.- (a) Schematic demagnetization curves for an exchange spring magnet and a conventional magnet and (b) schematic representation of the reversibility of the magnetic moments.

conjunction with a high remanence and a high coercivity distinguishes them uniquely from the conventional single ferromagnetic phase permanent magnets, where the demagnetization curves reflect essentially the distribution of the critical switching fields and are, therefore, mainly irreversible.

Schrefl et al. [9] used a finite element method to analyse a hard–soft composite structure with soft phase grains embedded in the hard phase matrix and concluded that in order to introduce magnetic hardness from the hard phase into the soft magnetic regions, a size of the soft phase region smaller than twice the domain wall width of the hard phase is required. Another result of their calculations was a value above 0.5 on the saturation remanence ratio ($m_r = M_r/M_s$).

Skomski and Coey [10] obtained a similar conclusion about soft phase critical dimension and calculated that in an ideal $\text{Sm}_2\text{Fe}_{17}\text{N}/\text{FeCo}$ multilayer nanocomposite structure could be possible to archive an energy product of 120 MGOe.

1.2.4. Commercial magnets available.

Nowadays permanent magnets used in industry applications are classify by its performance (high coercivity and $(BH)_{\text{max}}$), this hard magnetic properties are strongly related with the content of Dy. As shown in Figure 1.14, an addition of 12 weight % of Dy in new permanent magnets allows to obtain a coercivity more than twice of a magnet without Dy, reaching values of $H_c = 35$ kOe. Depending on the application the magnet is

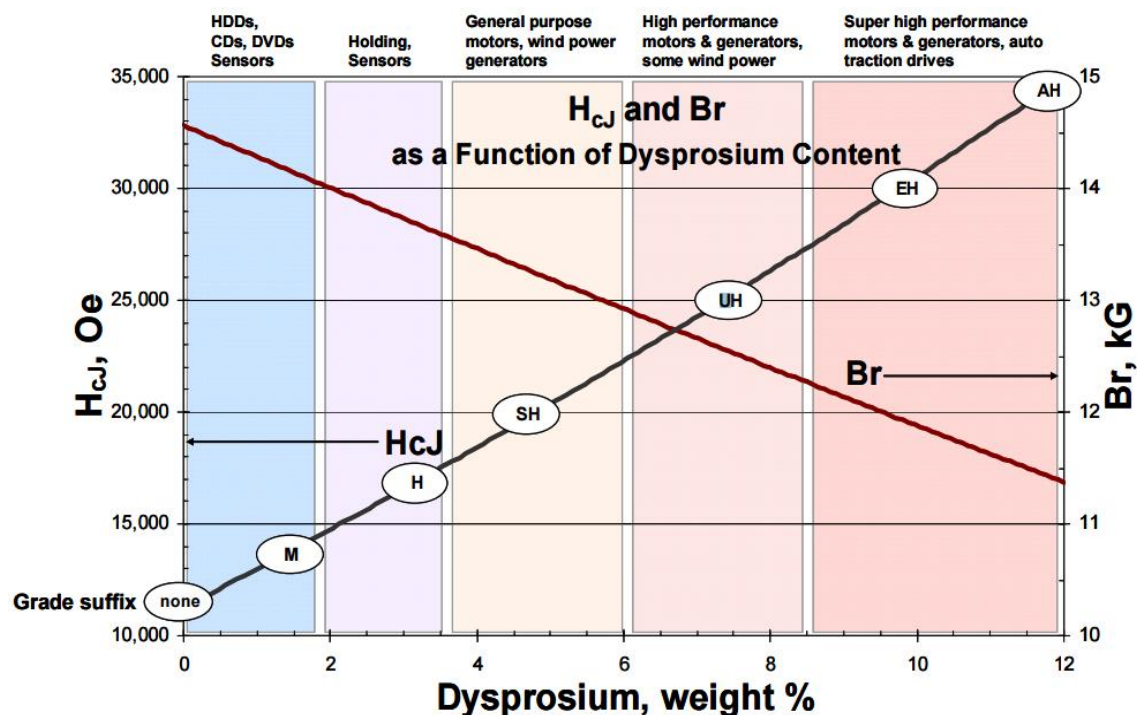


Figure 1.14.- Coercivity (H_{cJ}) and Residual Induction (B_r) as a function of dysprosium content. On top, applications for each grade [23].

build it, for example; for DVDs and HDDs sensors a Dy content less than 2 weight % is used during fabrication. The best magnet, used for super high performance motors and generators employs up to 12 weight % of this heavy rare earth element.

1.3. Objectives.

The main objective on this project is to find the best route in order to obtain a large coercivity enhancement of the Nd-lean samples by infiltrating a PrCuCo eutectic alloy. In order to accomplish this, the first task is to find the optimal initial microstructure by means of different heat treatments to the initial amorphous ribbons, looking for the greatest coercivity. Once the desired microstructure is found, a PrCoCu eutectic alloy will be infiltrated at 600 °C for different times with the aim to obtain an enhancement of the coercivity.

2. Experimental methodology.

2.1. Fabrication techniques.

2.1.1. Arc-Melting & Melt-spinning.

Cast samples with composition $\text{Nd}_{10}\text{Fe}_{84}\text{B}_6$ and $\text{Nd}_{12}\text{Fe}_{81}\text{B}_6\text{Nb}_1$ were prepared by melting the pure constituents of Nd, Fe, B and Nb. In order to melt these elements an electric arc furnace (EAF) was used. This kind of furnaces uses the electric arc made when the inert gas in the chamber, in our case argon, is ionized due to the high potential difference between an electrode and a conductive melting pot, which allows very high temperatures close to 3000 °C.

Pieces of the cast samples were melted using an induction furnace and immediately quenched using the melt-spinning technique with a Cu-based rotor at wheel speeds of 20-26 m/s. The melt-spinning furnace is a technique that allows to obtain very high cooling rates, on the order of 10^4 - 10^7 kelvins per second, getting this way amorphous or highly disordered ribbons of the material. All this process was made under Ar atmosphere.

2.1.2. Thermal treatments.

The amorphous ribbons were subjected to thermal treatments in order to crystallize them. These treatments were made under vacuum in a furnace at different temperatures in the range of 600-750 °C and for different times in order to obtain the optimum magnetic properties. As the furnace employed was not able to make vacuum, the samples were introduced on quartz tubes and sealed under vacuum after a purging process with argon to avoid oxidation.

The best sample was mixed with the low melting point $\text{Pr}_3\text{Co}_{0.75}\text{Cu}_{0.25}$ eutectic alloy in a 5:1 proportion in order to infiltrate the PrCoCu into the grain frontiers. This mixture was made under argon controlled atmosphere at a glovebox and sealed under vacuum on a quartz tube. These mixed samples were heat treated at 600 °C for several times between 1-7 hours so that the PrCoCu alloy infiltrates around the grain boundaries.

2.2. Characterization techniques.

2.2.1. Differential thermal analysis (DTA).

Differential thermal analysis is a thermoanalytic technique similar to Differential Scanning Calorimetry (DSC). In DTA, identical thermal cycles are applied to the material under study and an inert reference, while recording any difference between sample

and reference temperatures. This differential temperature can be plotted against time or against temperature (DTA curve or thermogram). Exothermic and endothermic changes on the samples can be detected relative to the inert reference. Therefore, a DTA curve provides data on the transformations that have occurred on the sample during heating/cooling such as glass transitions, crystallization, melting and sublimation. The enthalpy change of these transformations can be obtained with the area under the DTA peak, and it's not affected by the heat capacity of the sample.

A DTA consists of a sample holder comprising thermocouples, sample containers, a ceramic or metallic furnace, a temperature programmer; and a recording system. The basic configuration is the two thermocouples are connected in a differential arrangement and connected to a high gain low noise differential amplifier. One thermocouple is placed in the sample under study and the other is placed in an inert material such as Al_2O_3 . As the temperature is increased, there will be a brief deflection of the voltage if the sample is undergoing a phase transition. This occurs because the input of heat will raise the temperature of the inert substance, but be incorporated as latent heat in the material changing phase.

The calorimeter used to study the nanocrystallization process and possible secondary phases formed during heat treatments (as α -Fe) on amorphous ribbons was a SETARAM 92-16.18 with simultaneously differential thermal analysis (DTA) and thermogravimetric analysis (TGA) measurements. Experimental procedure to obtain this thermograms under Ar atmosphere was as follows; first heating and then cooling at 10 K/min from 20 °C and up to 800 °C to check irreversible process during thermally induced crystallization

2.2.2. X-ray diffraction (XRD)

X-ray diffraction is nowadays one of the most common techniques for the study of crystal structures. X-ray diffraction is based on constructive interference of monochromatic X-rays and a crystalline sample. These X-rays are generated by a cathode ray tube, filtered to produce monochromatic radiation, collimated to concentrate, and directed toward the sample. The interaction of the incident rays with the sample produces constructive interference (and a diffracted ray) when conditions satisfy Bragg's Law ($n\lambda=2d \sin \theta$). This law relates the wavelength of electromagnetic radiation to the diffraction angle and the lattice spacing in a crystalline sample. These diffracted X-rays are then detected, processed and counted. When using a powder sample, scanning it through a range of 2θ angles, all possible diffraction directions of the lattice should be attained due to the random orientation of the powdered material. To avoid possible crystal preference directions, the sample holder can be coupled to a rotor (spinner), assuring the random orientation.

The XRD measurements have been made on a Philips X'Pert Pro diffractometer from x-rays general service of the UPV/EHU. This diffractometer uses a Bragg-Brentano θ - θ geometry, along 5° and 80° (2θ) with $\Delta(2\theta) = 0.026269^\circ$ steps. The samples were located on a spinner as they were obtained after the heat treatments. A Cu anode is used as X-ray source and a monochromator to select the K_α line with $\lambda = 1.5418 \text{ \AA}$.

The diffractograms obtained have been refined using the FullProf suite by a pattern matching and following Rietveld methods in order to obtain the ratio of phases in the samples, and a single peak was analysed using the Scherrer equation (Equation 2.1) to obtain an estimation of the grain size.

$$D = \frac{K\lambda}{\beta \cos\theta} \quad (2.1)$$

where D is the mean size of ordered crystalline domains, which may be smaller or equal to the grain size, K is a shape factor with a value close to unity, a typical value used is 0.94, λ is the X-ray wavelength, β is the full width at half maximum (FWHM) and θ is the Bragg angle.

2.2.3. Vibrating sample magnetometer (VSM)

A VSM is a scientific instrument used to measure the magnetization of materials under test. The Figure 2.1 shows the schematic basic operation of this system: a sample is placed within a uniform magnetic field H that induces a magnetization in the sample while a perpendicular oscillation movement is realized by the sample, normally by means of a piezoelectric or a lineal actuator. This vibration induces a voltage on the pickup coils proportional to the magnetic moment of the sample, and independent of the applied magnetic field.

In this project, two VSM have been used. The first is a homemade VSM with a modified configuration from a commercial VSM. This modification has the purpose of incorporate automatic data acquisition techniques and instrumentation control through LabVIEW programming. The maximum magnetic field accessible with this VSM is 1.8 T and can operate at temperatures between 150-1000 K thanks to a furnace. The second system is a high field VSM (HF-VSM) that has a He closed circuit refrigerated superconductor magnet that allow measurements between 2-325 K and magnetic fields up to 14 T.

These two VSMs have been used to trace the hysteresis loops of the samples, the VSM of 1.8 T for the crystalized ribbons without diffusion and the HF-VSM of 14 T for the diffused samples in order to reach the saturation.

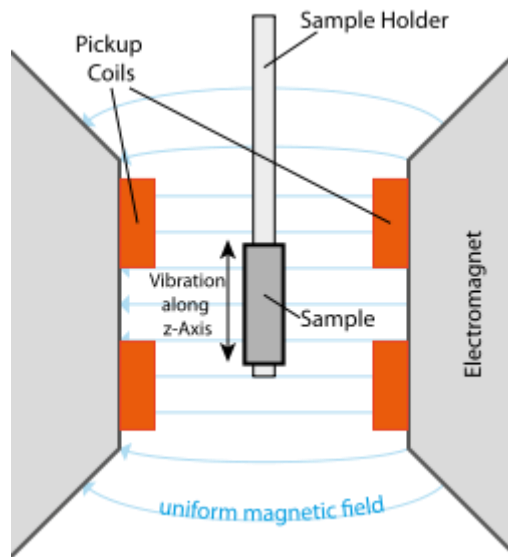


Figure 2.1.- Schematic basic operation of a VSM.

2.2.4. Scanning transmission electron microscopy (STEM)

The STEM is a type of transmission electron microscope (TEM) that combines the principles of transmission electron microscopy and scanning electron microscopy. The STEM requires very thin samples and looks primarily at beam electrons transmitted by the sample like the TEM. One of its advantages over TEM is enabling the use of other signals that cannot be spatially correlated in TEM. Like secondary electrons, scattered beam electrons, characteristics X-ray and electron energy loss.

Like SEM, the STEM technique scans a very finely focused beam of electrons across the sample in a raster pattern. Interactions between the beam electrons and sample atoms generate a serial signal stream, which is correlated with beam position to build a virtual image in which the signal level at any location in the sample is represented by the grey level at the corresponding location in the image. Its primary advantage over conventional SEM imaging is the improvement in spatial resolution.

For this project we have obtained images of the microstructure of the samples using a configuration of a normal TEM. We have obtained images using the method of high-angle annular dark-field imaging (HAADF), this method uses a detector to collect transmitted beam electrons that have been scattered through a relatively large angle, being highly sensitive to variations in the atomic number of elements in the sample. An energy-dispersive X-ray spectroscopy (EDS) analysis was also made. This technique analyses the X-rays emitted by the sample when bombarded with an electron beam. These X-rays have a characteristic energy for each element, allowing us to analyse the spatial composition of the sample.

3. Results & Discussion

3.1. Nanocrystalline hard magnets.

In order to obtain nanocrystalline ribbons, it is necessary to know at which temperature the amorphous ribbons must be treated to crystallize them. With this intention a differential thermal analysis (DTA) was made. The curves obtained in this process for the $\text{Nd}_{10}\text{Fe}_{84}\text{B}_6$ and $\text{Nd}_{12}\text{Fe}_{81}\text{B}_6\text{Nb}_1$ compositions are shown in Figure 3.1.

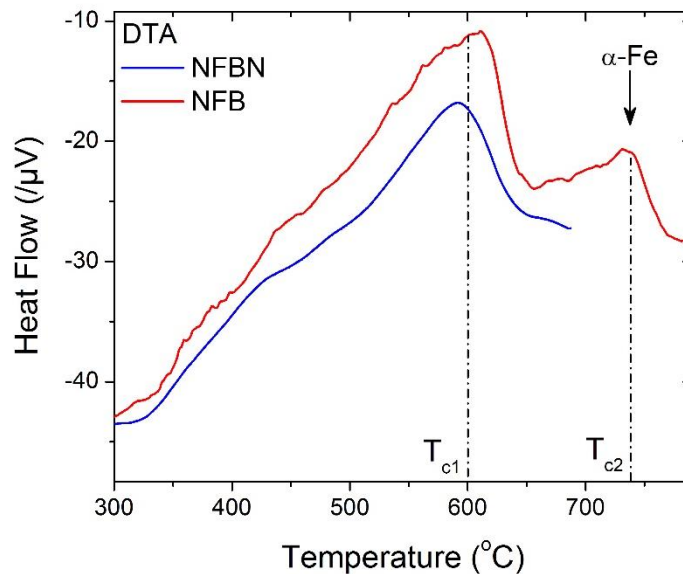


Figure 3.1.- DTA curve for the compositions $\text{Nd}_{10}\text{Fe}_{84}\text{B}_6$ (red line) and $\text{Nd}_{12}\text{Fe}_{81}\text{B}_6\text{Nb}_1$ (blue line).

The curves from the DTA show two exothermic peaks. The first peak, corresponding with an approximate temperature of $T_{c1} = 600\text{ }^\circ\text{C}$, corresponds to the crystallization of the $\text{Nd}_2\text{Fe}_{14}\text{B}$ phase, while the second peak, appearing at an approximated temperature of $T_{c2} = 730\text{ }^\circ\text{C}$, corresponds to the crystallization of the bcc structure of iron, the $\alpha\text{-Fe}$ phase.

With these results in mind, the heat treatment for the crystallization of amorphous ribbons must be done in between the temperatures of both crystallization process with the intention to obtain $\text{Nd}_2\text{Fe}_{14}\text{B}$ grains with specific sizes and without excessive $\alpha\text{-Fe}$ phase. It is important to control the temperature and time of the heat treatment to achieve $\text{Nd}_2\text{Fe}_{14}\text{B}$ grains with a specific range of sizes as this is known to affect the coercivity [11]. The coercivity of powdered magnets increases with the reduction of particle size going through a maximum at the single domain size and then decreases again for ultrafine particles due to thermal effects and becomes zero at the superparamagnetic particle size (Figure 3.3).

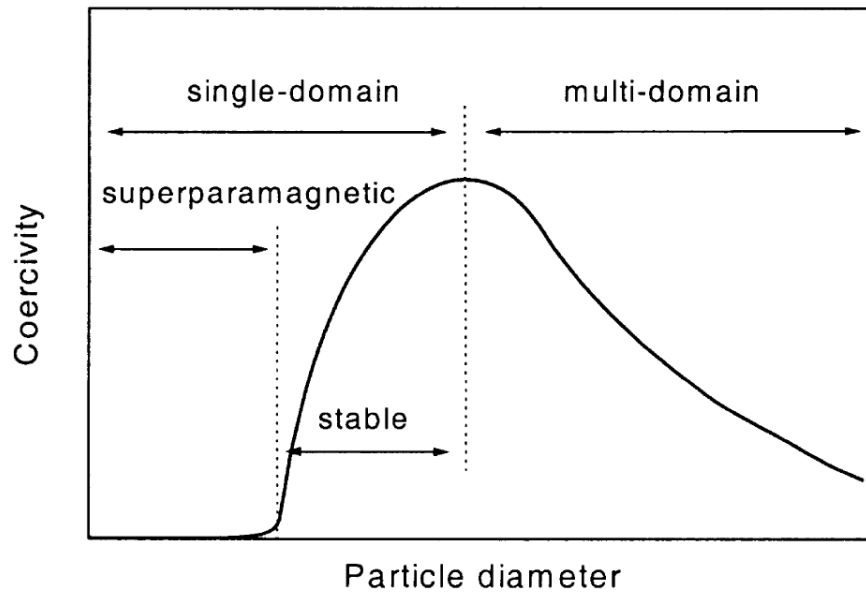


Figure 3.3.- Size dependence of coercivity [13].

According with this, in order to have the widest coercivity, heat treatments were defined to achieve an $\text{Nd}_2\text{Fe}_{14}\text{B}$ grain size close to the single domain size limit. For $\text{Nd}_2\text{Fe}_{14}\text{B}$ phase, this single domain size limit is reported to be between 250-300 nm [12]

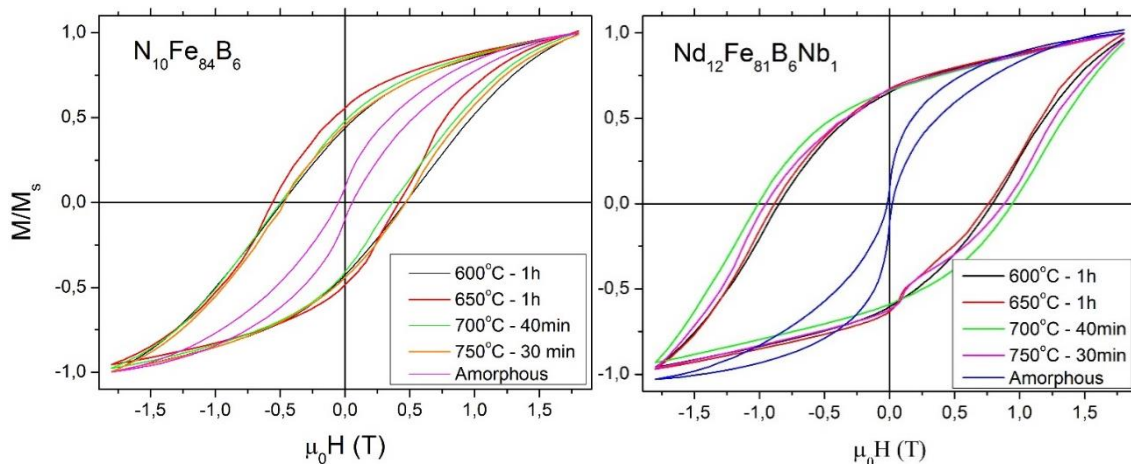


Figure 3.2.- Hysteresis loops of the amorphous and nanocrystalline ribbons. Left: $\text{Nd}_{10}\text{Fe}_{84}\text{B}_6$ composition, right: $\text{Nd}_{12}\text{Fe}_{81}\text{B}_6\text{Nb}_1$ composition.

[13].

Hysteresis loops of the amorphous/highly disordered and heat treated nanocrystalline samples were obtained by VSM with a magnetic field up to 1.8 T (Figure 3.2). Despite the fact that these hysteresis loops are minor loops (they are not symmetric), a huge change in coercivity is seen between the amorphous ribbons and the heat treated ones, confirming the crystallization of the $\text{Nd}_2\text{Fe}_{14}\text{B}$ hard phase, while the saturation remanence ratio is above 0.5 for all the $\text{Nd}_{12}\text{Fe}_{81}\text{B}_6\text{Nb}_1$ composition samples while it is only above 0.5 for the 650°C heat treated sample of the $\text{Nd}_{10}\text{Fe}_{84}\text{B}_6$ composition. This

value above 0.5 is expected for nanocomposite exchange-coupled magnets as mentioned in section 1.2.3.

The shape of the amorphous ribbons hysteresis loops may be that of a mixture of an amorphous/disordered magnetic phase, with very small $\text{Nd}_2\text{Fe}_{14}\text{B}$ crystals, but they were not actually analysed as they were not important to the development of this work.

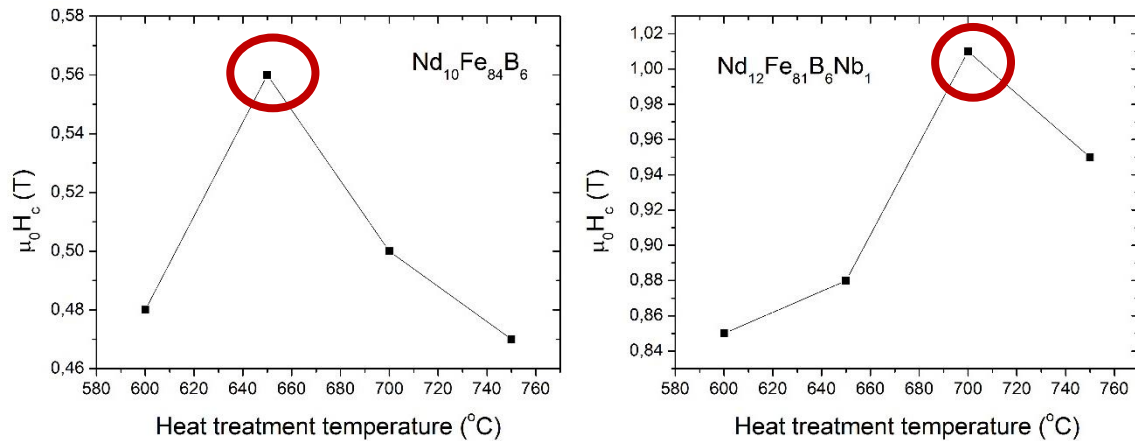


Figure 3.4.- Coercive field of the different heat treated samples. Left: $\text{Nd}_{10}\text{Fe}_{84}\text{B}_6$ composition, right: $\text{Nd}_{12}\text{Fe}_{81}\text{B}_6\text{Nb}_1$ composition.

The evolution of the coercive field of the heat treated samples with the temperature is shown in Figure 3.4. Samples displayed a maximum value of the coercivity of 0.56 T at a temperature of 650 °C for the $\text{Nd}_{10}\text{Fe}_{84}\text{B}_6$ composition and of 1.01 T at a temperature of 700 °C for the $\text{Nd}_{12}\text{Fe}_{81}\text{B}_6\text{Nb}_1$ composition. The shape of the dependence of coercivity with the heat treatment can be related to the change of size of the $\text{Nd}_2\text{Fe}_{14}\text{B}$ grain sizes. As the heat treatment temperature increases, so does the grains sizes. Comparing with Figure 3.3, the samples with the maximum coercivity should be near the single domain limit size, while the lower coercivity at higher temperatures is associated with the formation of multidomain grains and at lower temperatures with the thermal effects on finer grains.

The nanocrystalline samples with maximum coercivity were analysed by XRD prior the diffusion process. The diffractograms of these samples are shown in Figure 3.5.

Looking at the angle corresponding to the α -Fe phase peak it is clear that in the composition of $\text{Nd}_{12}\text{Fe}_{81}\text{B}_6\text{Nb}_1$ its intensity ratio with the peaks from the $\text{Nd}_2\text{Fe}_{14}\text{B}$ phase is much lower than that of the composition $\text{Nd}_{10}\text{Fe}_{84}\text{B}_6$. The Rietveld refinement of these samples indicates that for the $\text{Nd}_{10}\text{Fe}_{84}\text{B}_6$ composition the percentage of α -Fe phase is 42.58% while for the $\text{Nd}_{12}\text{Fe}_{81}\text{B}_6\text{Nb}_1$ composition is only 4.81%. This lack of α -Fe phase is due to the stoichiometry of the composition, using all the Fe in the formation of the $\text{Nd}_2\text{Fe}_{14}\text{B}$ phase.

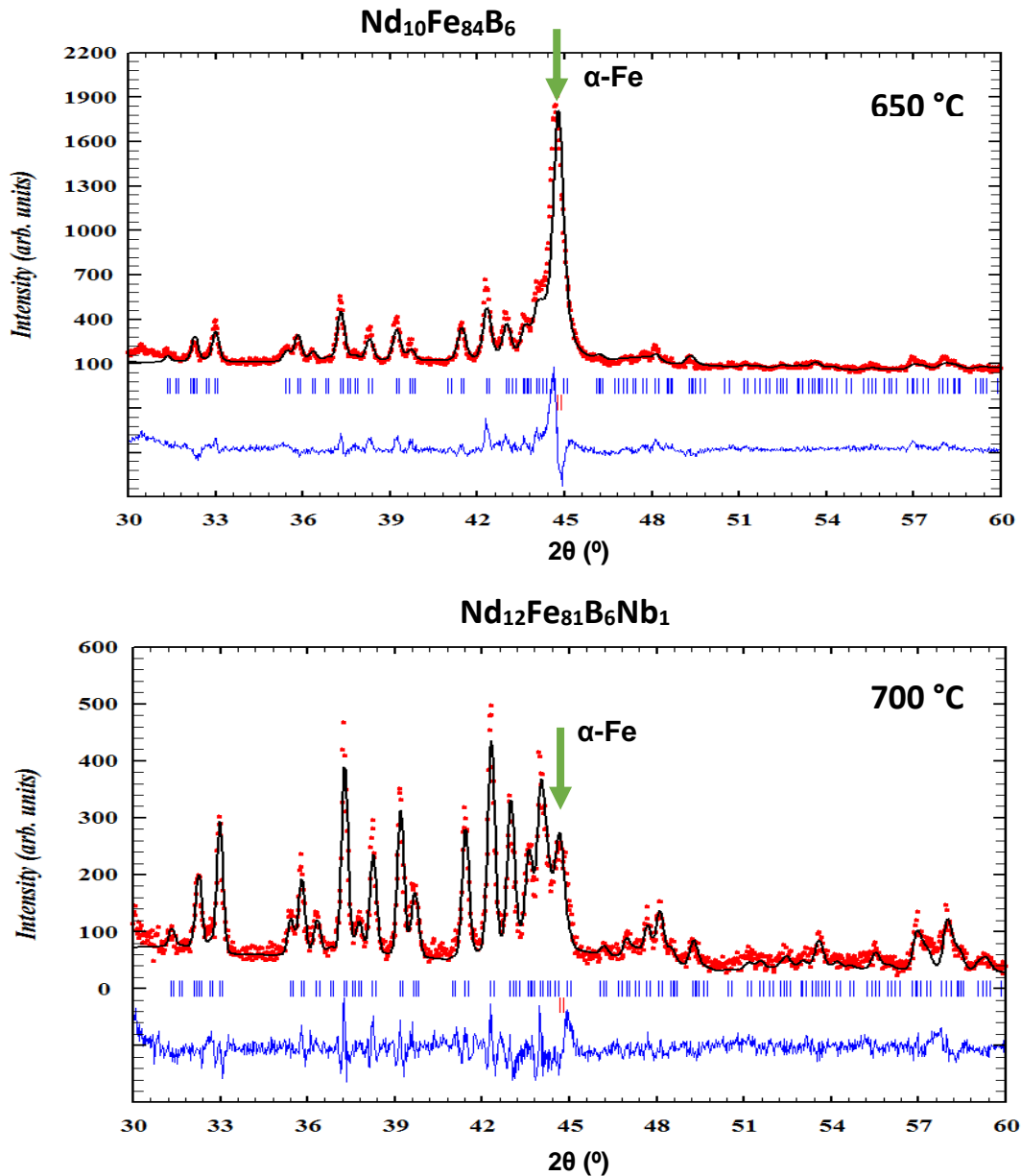


Figure 3.5.- Diffractograms of the samples heat treated at $650\text{ }^\circ\text{C}$ of $\text{Nd}_{10}\text{Fe}_{84}\text{B}_6$ (up) and at $700\text{ }^\circ\text{C}$ of $\text{Nd}_{12}\text{Fe}_{81}\text{B}_6\text{Nb}_1$ (down). The peak corresponding with the $\alpha\text{-Fe}$ phase is indicated.

The peak at 2θ around 37.25° was analysed by the Scherrer's formula (Equation 2.1) to estimate the grain size. The estimated grain size of the $\text{Nd}_{10}\text{Fe}_{84}\text{B}_6$ composition is 80 nm while for the $\text{Nd}_{12}\text{Fe}_{81}\text{B}_6\text{Nb}_1$ is 77 nm. Another estimation of these sizes was obtained with the Rietveld refinement that gave a value of 110 nm for the $\text{Nd}_{10}\text{Fe}_{84}\text{B}_6$ composition and 68 nm for the $\text{Nd}_{12}\text{Fe}_{81}\text{B}_6\text{Nb}_1$ composition.

These two samples were chosen to make the diffusion process, but this was only possible on the $\text{Nd}_{10}\text{Fe}_{84}\text{B}_6$ composition. When trying to make the diffusion onto the $\text{Nd}_{12}\text{Fe}_{81}\text{B}_6\text{Nb}_1$ composition samples, the PrCoCu alloy stayed as it was before the heat treatment. This diffusion problem may be related to the very small amount of $\alpha\text{-Fe}$ phase in the sample and must be further studied.

3.2. Coercivity enhancement by grain boundary engineering.

3.2.1. Magnetic properties.

The hysteresis loops of the samples after the diffusion of the PrCoCu alloy are represented in Figure 3.6.a.

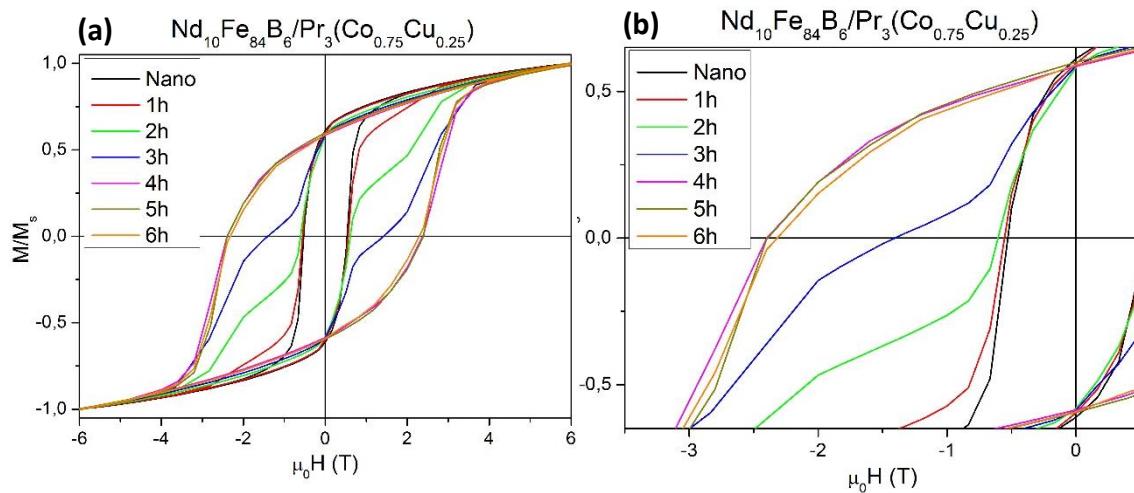


Figure 3.6.- (a) Hysteresis loops of the infiltrated samples after different diffusion treatment times at 600 °C and (b) detailed demagnetization curves.

The shape of the sample diffused during 1 hour indicates that the PrCoCu alloy has not diffused along the sample as it remains almost the same as the nanocrystalline sample. With increasing infiltration time part of the sample develops a higher coercivity as seen by the higher inflection point on the demagnetization curve. The characteristic bottle neck shape in the hysteresis loops on 2 and 3 hours diffused samples indicates a coarse mixture of the soft and hard phases and therefore a decoupled composite.

Focusing on the demagnetization curves (Figure 3.6.b) is possible to see the huge increment of coercivity from the nanocrystalline sample and up to the diffused samples during 4, 5 and 6 hour while the remanence saturation ratio decreases a little bit.

The remanence saturation ratio decreases with the diffusion time as shows Figure 3.7. This decrease is due to the addition of the non-magnetic PrCoCu alloy, but despite this decrease, the remanence saturation ratio stays above 0.5 reaching a minimum value of 0.55833 for the 2 hours diffused sample, going up to 0.5998 for the 5 hour diffusion time sample. This rise could be related to a less amount of PrCoCu diffused into the sample but better dispersed along the grain boundaries as the coercive field has the same value for the three last samples (Figure 3.9).

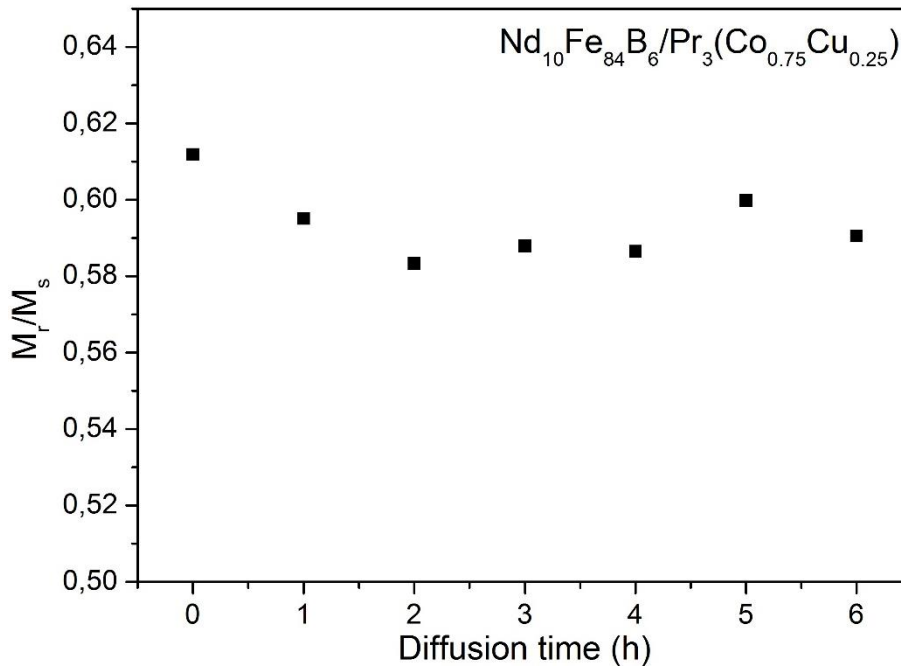


Figure 3.7.- Evolution of the remanence saturation ratio with the diffusion process time.

The nature of the interactions in a set of magnetic nanoparticles has been determined by using the Wohlfarth relationship established for non-interacting single-domain uniaxial nanoparticles, $m_d = 1 - 2m_r$ [14]. A deviation from the Wohlfarth relationship is an indication that the nanoparticles are interacting among themselves. The deviation is better seen through a relationship known as δm and defined as $\delta m = m_d(H) - [1 - 2m_r(H)]$ [15].

The δm curves of the nanocrystalline and 4 hours diffused samples were built using the magnetizing $M_r(H)$ and demagnetizing $M_d(H)$ remanent magnetizations measured as follows. First, the isothermal remanent magnetization $M_r(H)$ is measured after a magnetic field $H(H>0)$ is applied and removed. This procedure is repeated with the magnitude of H being gradually increased until the magnetization reaches saturation ($H=H_{sat}$). Next, the remanent demagnetizing magnetization is obtained following a somewhat similar procedure. Starting from the maximum remanence, e.g., after the sample has been saturated and H_{sat} has been removed, one applies and removes a negative field ($H<0$) and measures the remanence. H is then gradually increased toward (negative) saturation. It is important to use the same values of H in both procedures to allow a good correlation between both remanent magnetization data. Finally, $M_r(H)$ and $M_d(H)$ are normalized by the saturation remanence $M_r(H_{sat})$: $m_r = M_r(H)/M_r(H_{sat})$ and $m_d = M_d(H)/M_d(H_{sat})$.

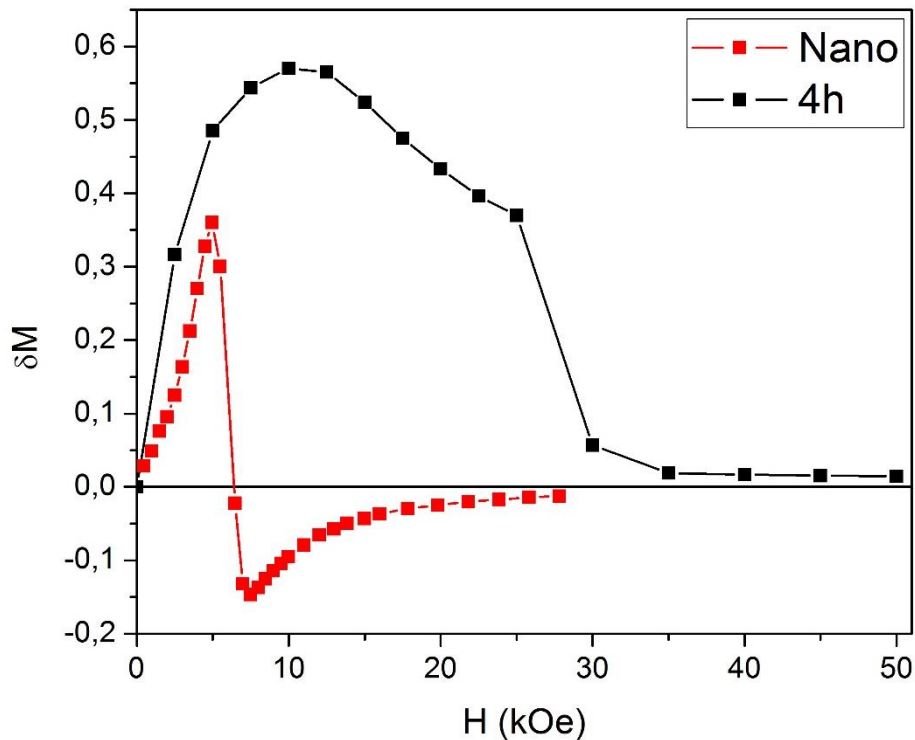


Figure 3.8.- δM curves for the nanocrystalline (red) and the 4 hours diffused (black) samples.

Figure 3.8 shows that for the nanocrystalline sample, initially values of δm are positive, indicating the existence of magnetizing (exchange-coupling) interactions between phases.

For the 4 hours samples the maximum of δm is larger indicating that the exchange-coupling interactions are stronger achieving a better coupling between phases.

Figure 3.9 shows that the coercivity of the samples increases almost 5 times from 0.52 T of the nanocrystalline sample to 2.4 T for the 4 and 5 hour diffused samples. This increase of the coercivity with the PrCoCu alloy diffusion along the grain boundaries is not yet fully understood. One point of view is that the modified boundary layers may cause a decrease of the nucleation field of reversed magnetic domain and this can lead to an enhancement in the coercivity [16] [17] [18] [19].

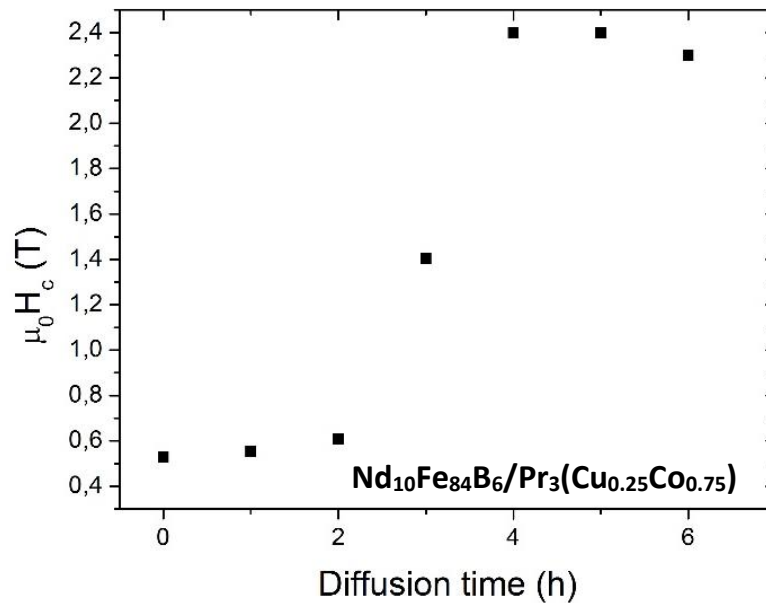


Figure 3.9.- Evolution of the coercivity with the diffusion process time.

Table 3.1 shows a comparison of the coercivity between different permanent magnets, both commercially available and from laboratory.

Table 3.1.- Comparison of coercivity from different permanent magnets, commercially available (c) and from laboratory (l).

Magnet composition	$\mu_0 H_c$ (T)	Reference
Nd ₁₀ Fe ₈₄ B ₆ /PrCoCu (5:1) (l)	2.4	This work
NdFeB/PrCu (7:3) (l)	2.4	Wan et al. [16]
Nd _{14.4} Fe _{78.4} Co _{1.3} B _{5.9} /DyF (l)	0.85	Ding et al. [17]
NdFeB/(DyO, DyF, TbF) (l)	1.5-2.4	Hirota et al. [20]
Nd ₁₃ Fe _{79.4} B ₇ Nb _{0.3} Ga _{0.3} /PrCu (l)	1.8	Lin et al. [21]
Nd _{10.9} Pr _{3.1} Fe _{77.4} Co _{2.4} B ₆ Ga _{0.1} Cu _{0.1} /Dy (l)	2.05	Sepehri-Amin et al. [18]
Nd ₉ Fe ₈₅ B ₆ /Nd (20:3) (l)	0.41	Wang et al. [22]
NdFeBAlNbDy (c)	1.1-3.5	Constantinides [23]

Commercial magnets are divided in grades (M, H, SH, UH, EH and AH) depending on the amount of dysprosium that they have in the range from 2 to 12 weight percent. The magnets with greater coercive field are those with 12 weight % of dysprosium, reaching a value of 3.5 T. Comparing with the magnets obtained during this work, the magnets corresponding with a coercive field around 2.4 T are from grade SH or UH with a minimum H_c of 2.0 and 2.5 T respectively. These commercial magnets use between 4-8

weight % of dysprosium and are used for general purpose motors, wind power generators and High performance motors & generators as seen in Figure 1.14.

3.2.2. Microstructure.

The ratio of phases present in the samples was obtained from the X-ray diffractograms of the diffused samples (Figure 3.10) by a Rietveld refinement with the FullProf suite. The phases analysed were $\text{Nd}_2\text{Fe}_{14}\text{B}$, $\alpha\text{-Fe}$ and PrCu .

On Table 3.2 is shown the amount of $\alpha\text{-Fe}$ phase in each sample. With the exception of the 1 hour diffused sample, there is a decreasing tendency of the amount of this phase as the diffusion time increases. The value of 0% for the 6 hours diffused samples is not very confident as the X-ray diffractogram of that sample is very noisy and the refinement was not very fine.

Table 3.2.- Amount of $\alpha\text{-Fe}$ phase in the different diffused samples.

Diffusion time	0h	1h	2h	3h	4h	6h
$\alpha\text{-Fe}$ %	42.58	50.42	36.59	26.96	19.34	0

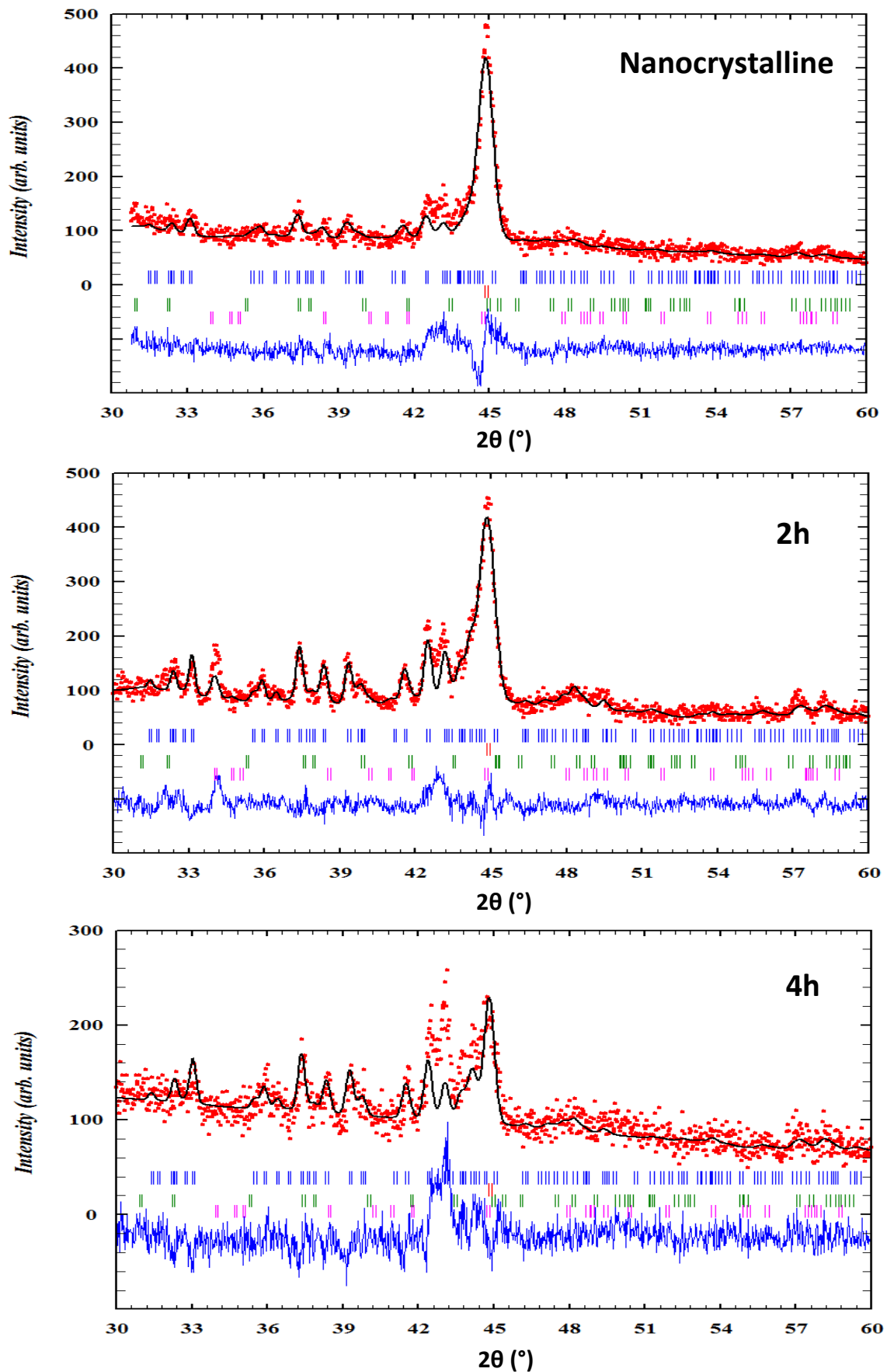


Figure 3.10.- XRD diffractograms refined with FullProf of the nanocrystalline sample (top), the 2 hour diffused sample (middle) and the 4 hours diffused sample (down). Analysed phases: $\text{Nd}_2\text{Fe}_{14}\text{B}$ (blue), $\alpha\text{-Fe}$ (red) and PrCu (green).

The samples diffused for 4 hours were sent to the University of Delaware in order to analyse them with a scanning transmission electron microscopy (STEM). Figure 3.12 shows TEM images of the sample. These images show grains with size 100-150 nm. This size is similar to that estimated in the nanocrystalline sample (210 nm) and it is below the single domain critical size for the $\text{Nd}_2\text{Fe}_{14}\text{B}$ crystals [12] [13].

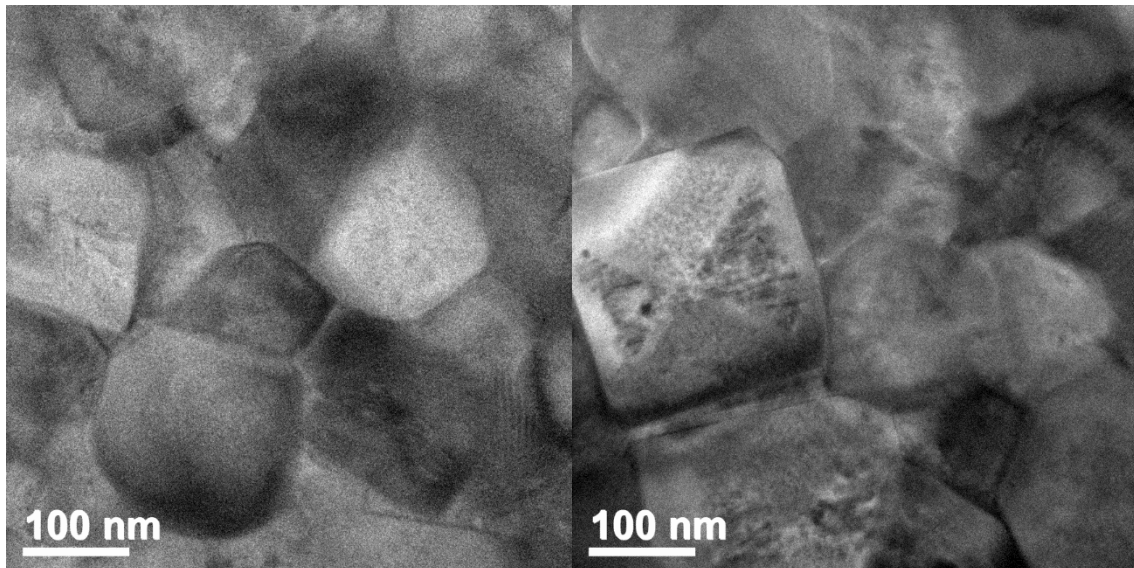


Figure 3.12.- TEM images of the sampled diffused for 4 hours.

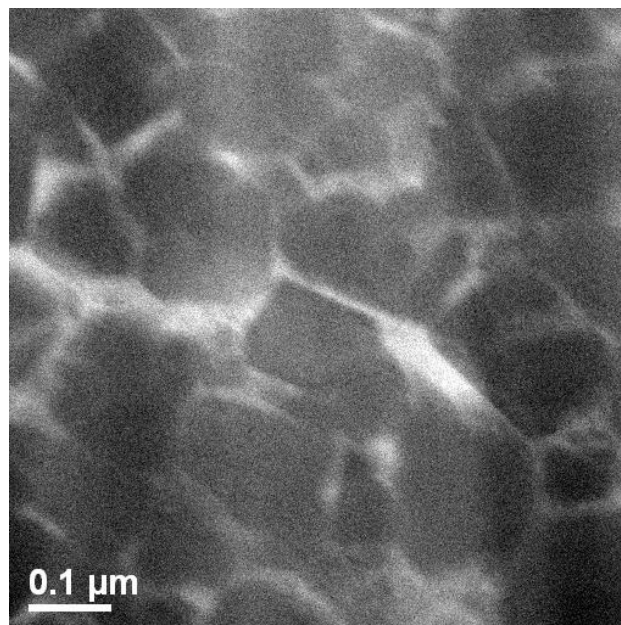


Figure 3.11.- High angular annular dark-field image (STEM-HAADF) of the 4 hours diffused sample.

Figure 3.11 shows the image obtained by high angular annular dark-field imaging (STEM-HAADF). The clear bright contrast at the grain boundaries indicates the formation of a rare-earth rich phase.

The elemental mapping made by energy-dispersive X-ray spectroscopy (EDS) shows that this rare-earth rich phase corresponds to the PrCoCu alloy diffused along the grain boundaries, while the Fe is distributed inside the grains.

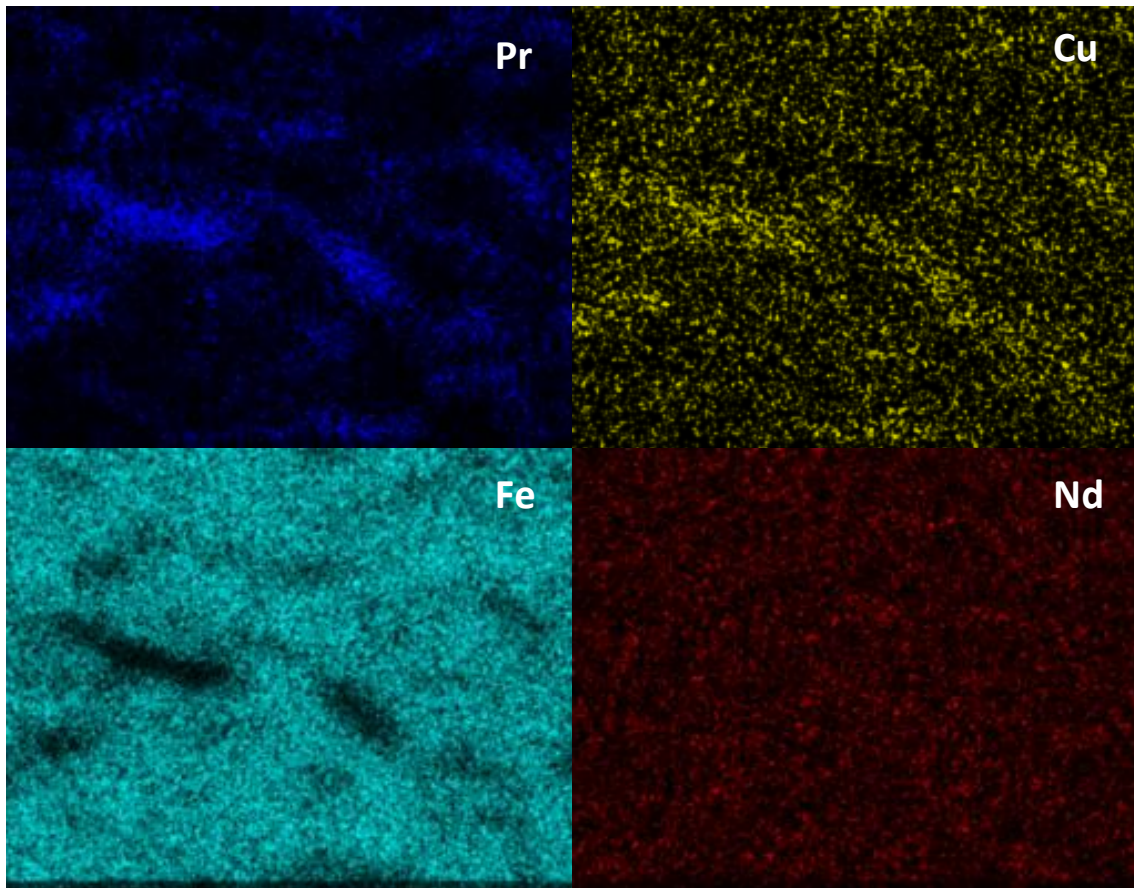


Figure 3.13.- STEM-EDS elemental mapping images of the 4 hours diffused sample.

4. Conclusions.

In this work, the crystallization of the $\text{Nd}_{10}\text{Fe}_{84}\text{B}_6$ and $\text{Nd}_{12}\text{Fe}_{81}\text{B}_6\text{Nb}_1$ amorphous/disordered ribbons was studied in order to obtain the optimum microstructure which was used later to diffuse the PrCoCu eutectic alloy to achieve an enhancement of the coercivity. From the results obtained in the characterization of these permanent magnets, the following conclusions are highlighted:

- In order to obtain a good diffusion of the PrCoCu alloy along the grain boundaries it is important to have an adequate amount of α -Fe. The diffusion was not completed in the $\text{Nd}_{12}\text{Fe}_{81}\text{B}_6\text{Nb}_1$ composition ribbons as a result of the lack of α -Fe phase, with only a 4.81% versus the amount of 42.58% in the $\text{Nd}_{10}\text{Fe}_{84}\text{B}_6$ composition ribbons, in which the PrCoCu were diffused without problems.
- It A drastic increase of almost 5 fold of the coercivity was observed related to the grain boundary diffusion of the PrCoCu alloy. This increase, reaching the value of 2.4 T, places these magnets along those commercially available with a content of 4-8 % of dysprosium, reaching coercivity values required for wind power generators.
- The saturation magnetization decreases because of the addition of nonmagnetic PrCoCu material.
- The remanence saturation ratio is slightly decreased possibly due to the reduction of exchange-coupling. Despite this decrease, the samples remain above the 0.5 value.
- Electron microscopy images shows grain sizes of 100-150 nm, what is below the single domain critical size, allowing a greater coercivity in the nanocrystalline ribbons.
- The STEM-EDS elemental mapping shows that the PrCoCu alloy is located along the grain boundaries of $\text{Nd}_2\text{Fe}_{14}\text{B}$.

These results have led to an oral presentation at three conferences:

- Energy Materials Nanotechnology (EMN) Spain Meeting, San Sebastián, Spain, 2015. Regular oral presentation.
- 16th edition of IEEE Region 8 EuroCon, Salamanca, Spain, September of 2015. Regular oral presentation.
- International days in critical raw materials, Burgos, Spain, 2015. Invited oral presentation.

5. Bibliography

- [1] Arnold Magnetic Technologies Corp, "Permanent Magnet Applications Guide," 17 June 2015. [Online]. Available: http://www.arnoldmagnetics.com/Permanent_Magnet_Applications_Guide.aspx.
- [2] S. Chikazumi and S. Charap, *Physics of Magnetism*, New York: John Wiley and Sons, 1964.
- [3] P. Dent, "High performance magnet materials: Risky supply chain," *Advanced Materials and Processes*, vol. 167, no. 8, pp. 27-30, 2009.
- [4] R. Skomski and J. Coey, *Permanent Magnetism*, Bristol: Institute of Physics, 1999.
- [5] EU Ad-Hoc Working Group on Raw Materials, "Report on Critical Raw Materials for the UE," European Commission, 2014.
- [6] U.S. Department of Energy, "Critical Materials Strategy," U.S. Department of Energy, 2011.
- [7] E. Kneller and R. Hawig, "The exchange-spring magnet: a new material principle for permanent magnets," *IEEE Transactions on Magnetics*, vol. 27, no. 4, pp. 3588-3560, 1991.
- [8] R. Coehoorn, D. de Mooij and C. de Waard, "Meltspun permanent magnet materials containing Fe₃B as the main phase," *Journal of Magnetism and Magnetic Materials*, vol. 80, no. 1, pp. 101-104, 1989.
- [9] T. Schrefl, H. Kronmüller and J. Fidler, "Exchange hardening in nano-structured two-phase permanent magnets," *Journal of Magnetism and Magnetic Materials*, vol. 127, no. 3, pp. L273-L277, 1993.
- [10] R. Skomski and J. Coey, "Giant energy product in nanostructured two-phase magnets," *Physical Review B*, vol. 48, no. 21, pp. 15812-15816, 1993.
- [11] A. Morrish, *The Physical Principles of Magnetism*, New York: Wiley, 1965.
- [12] J. Livingston, "Magnetic Domains in Sintered FeNdB Magnets," *Journal of Applied Physics*, vol. 57, no. 8, pp. 4137-4139, 1985.

- [13] G. Hadjipanayis, "Nanophase Hard Magnets," *Journal of Magnetism and Magnetic Materials*, vol. 200, no. 1-3, pp. 373-391, 1999.
- [14] E. Wohlfarth, "Relations between Different Modes of Acquisition of the Remanent Magnetization of Ferromagnetic Particles," *Journal of Applied Physics*, vol. 29, no. 3, pp. 595-596, 1958.
- [15] P. Kelly, K. O'Grady, P. Mayo and R. Chantrell, "Switching Mechanisms in Cobalt-Phosphorus Thin Films," *IEEE Transactions on Magnetics*, vol. 25, no. 5, pp. 3881-3883, 1989.
- [16] F. Wan et al., "Coercivity enhancement of anisotropic die-upset Nd-Fe-B powders by Pr-Cu alloy diffusion," *Journal of Applied Physics*, vol. 113, no. 19, p. 193902, 2013.
- [17] Y. Ding, R. Chen, Z. Liu, D. Lee and A. Yan, "Coercivity enhancement of sintered Nd_{14.4} Fe_{78.4} Co_{1.3} B_{5.9} magnets by dysprosium diffusion in grain boundaries of rapidly solidified strips," *Journal of Applied Physics*, vol. 107, no. 9, p. 09A726, 2010.
- [18] H. Sepehri-Amin, T. Ohkubo and K. Hono, "The mechanism of coercivity enhancement by the grain boundary diffusion process of Nd-Fe-B sintered magnets," *Acta Materialia*, vol. 61, no. 6, pp. 1982-1990, 2013.
- [19] X. Tang et al., "Impact of Nd-Cu diffusion on microstructure and coercivity in hot-pressed and die-upset nanocomposite magnets," *Scripta Materialia*, vol. 88, pp. 49-52, 2014.
- [20] K. Hirota, H. Nakamura, T. Minowa and M. Honshima, "Coercivity Enhancement by the Grain Boundary Diffusion Process to Nd-Fe-B Sintered Magnets," *IEEE Transactions on Magnetics*, vol. 49, no. 10, pp. 2909-2911, 2006.
- [21] Z. Lin et al., "Improvement of coercivity and thermal stability of anisotropic Nd₁₃Fe_{79.4}B₇Nb_{0.3}Ga_{0.3} powders by diffusion of Pr-Cu alloys," *Applied Physics Letters*, vol. 100, no. 5, p. 052409, 2012.
- [22] Y. Wang et al., "Coercivity enhancement of Nd₂Fe₁₄B/a-Fe nanocomposite magnets through neodymium diffusion under annealing," *Journal of Rare Earths*, vol. 30, no. 8, pp. 757-760, 2012.
- [23] S. Constantinides, "The Important Role of Dysprosium in Modern Permanent Magnets," 17 January 2012. [Online]. Available:

<http://www.arnoldmagnetics.com/WorkArea/linkit.aspx?LinkIdentifier=id&ItemID=5701&libID=5803>. [Accessed 21 June 2015].

- [24] S. Shawn and S. Constantinides, "Permanent magnets: the demand for rare earths," in *8th Int Rare Earths Conference*, Hong Kong, 2012.
- [25] M. Humphries, "Rare Earth Elements: The Global Supply Chain," Congressional Research Service, 2013 .
- [26] B. Culity and C. Graham, *Introduction to Magnetic Materials*, New Jersey: John Wiley & Sons, Inc., 2009.
- [27] E. Furlani, *Permanent Magnet and Electromechanical Devices*, New York: Academic Press, 2001.
- [28] N. A. Spaldin, *Magnetic Materials: Fundamentals and Applications*, New York: Cambridge University Press, 2011.